בס"ד

מכון ויצמן למדע
WEIZMANN INSTITUTE OF SCIENCE

עבודת גמר (תזה) לתואר
דוקטור לפילוסופיה

מוגשת למועצה המדעית של
מכון ויצמן למדע
רחובות, ישראל

מאת
אייל כהן-חושן

אינטראקציות של אקסיטון ופלסמון בננו-מבנים של זהב
ונקודות קוונטיות

Thesis for the degree
Doctor of Philosophy

Submitted to the Scientific Council of the
Weizmann Institute of Science
Rehovot, Israel

By
Eyal Cohen-Hoshen

Exciton-Plasmon Interactions in Gold and
Quantum Dot Nanostructures

מנחה:
פרופסור ישראל
בר-יוסף

Advisor:
Professor Israel
Bar-Joseph

סיון ה'תשע"ד

June, 2014

Localized Surface Plasmons (LSPs) are excitations of the electromagnetic field in sub-diffraction limit volume of metals, which have a negative dielectric function. These excitations induce a large electromagnetic field in a very small volume. Interactions of plasmons with optically active materials like molecules or quantum dots (QDs) result in pronounced modification of their absorption and emission properties. This work focuses on the interaction of plasmons and excitons in nanostructures made of gold nanoparticles (NPs) and CdSe/ZnS core-shell nanocrystals. The plasmon resonance frequency and intensity is governed by the type of metal and by the nanostructure size and shape while the exciton frequency, due to quantum confinement, depends on the QD size. In this work, by tuning the spectral and spatial overlap of these resonances we demonstrate the control of the optical properties of the hybrid structure.

We have developed reproducible methods for the synthesis of gold NPs by wet chemistry as well as by e-beam lithography. Using DNA and protein based self-assembly as well as top down methods, these NPs are assembled into structures together with semiconductor QDs. The resulting structures have a well defined QD-NP separation and well characterized plasmon resonance. Using these structures we have demonstrated the modification of the absorption and emission properties of the QD due to the strong exciton-plasmon interaction. The experimental findings of our work are shown to be consistent with theoretical models and provide solid explanation for many of the experimental ambiguities in this field.

We show that the absorption of the QD is enhanced by an order of magnitude for single QD-NP structures and up to two orders of magnitude for NP-QD-NP structure. Moreover, by changing the polarization of the excitation we are able to tune the spatial overlap of the plasmon and exciton resonances and observe a change of the absorption enhancement ranging from zero up to the maximal enhancement factor.

The amplified absorption is shown to depend on the spectral overlap of the plasmon and exciton resonances, and is evident in the modified photoluminescence excitation spectrum (PLE) of the QD. Lifetime measurements show that the decay rate of the exciton is enhanced by more than an order of magnitude when compared to bare QDs.

Acknowledgments

I wish to express my deepest gratitude to Professor Israel Bar-Joseph for his guidance. The many years we have been working together were inspiring. His door is always open for discussion and advice. He is open minded and let me lead my own way in research.

I will always remember the late Professor Yossi Sperling. The many years of collaborations were fun as much as they were fruitful. Although the many years separating us I see Yossi as a friend.

I would like to thank my colegues Yuval Vardi and Dr. Arjun Joshua and the past students at our research group: Avi Guttman, Michael Stern, Valery Garmider, Dan Mendels and Tali Dadosh. It has been a real pleasure to work together.

Finally I would like to thank my beloved Nurit who supported me all these years and gave me the space and time to flourish.

Contents

List of Abbreviations

QD	Quantum Dot
NP	Nanoparticle
LSP/LSPR	Localized Surface Plasmon Resonance
SERS	Surface Enhanced Raman Scattering
TM	Transverse Magnetic
TE	Transverse Electric
dsDNA/ssDNA	double/single stranded DNA
TEM	Transmission Electron Microscope
SEM	Scanning Electron Microscope
AFM	Atomic Force Microscope
CCD	Charge Coupled Device
PLE	Photoluminescence Excitation
PMMA	Poly(methyl methacrylate)
HSQ	Hydrogen Silsesquioxane
FWHM	Full Width at Half Maximum

Chapter 1

Introduction

Plasmons are collective oscillations of charge density in metals. These oscillations are driven by an external electromagnetic field, that can be created by either light or by fast moving electrons. We will start with an overview of the field of Plasmonics and give a theoretical background to the field. We will introduce the concept of plasmons in three categories: Volume plasmons, surface plasmons and localized plasmons. Subsequently, we will focus on the excitation of localized plasmons, distinguishing between excitation by a plane wave and by near field coupling to an emitting dipole. This will lay down a basis for describing exciton-plasmon interactions that will serve for understanding the different interaction mechanisms relevant for this work.

1.1 Overview of Plasmonics

The optical properties of metal nanoparticles (NPs) is not a new field of research, and goes back to the 19th century, when Faraday [1] was fascinated with the strong red color of colloidal gold solutions, and conducted experiments on their optical properties. Theoretical explanation of the phenomenon was given by Mie in 1908 in his work on the scattering of light by gold colloids (metal NPs) [2]. The connection of the optical properties of metal NPs to modes of free electron oscillation in metals, plasmons, was

understood in the 1950s with Ritchie's work on plasma losses by fast electrons in thin films[3].

The renewed interest in this field in started about 30 years ago, with the measurements of Surface Enhanced Raman Scattering (SERS). The Raman intensity of molecules on rough surfaces was found to be enhanced by more than eight orders of magnitude. The origin of this strong enhancement was found to be mainly due to excitation of localized plasmons in metal surfaces. It was found that localized plasmons induce a strong electromagnetic field in the range of a few nanometers around nanoscale surface edges, and this strong field enhances the Raman process. Since then, surface plasmons and localized surface plasmons (LSP) continued to be extensively investigated [4, 5].

Today, due to recent advances that allow metals to be structured and characterized on the nanometer scale, researchers are able to control plasmon properties, reveal new aspects of their underlying nature and tailor them for specific applications [6].

Plasmonics has evolved into several directions, driven by different motivation, either applicative or fundamental. A large effort is devoted to the use of surface plasmon excitation for detection of specific biological binding. Another direction is to try to overcome the optical diffraction limit, by focusing and guiding light in sub-diffraction limit areas through the use of nanostructured surfaces. Here, the motivation is to produce new microscopy methods, and to produce plasmonics inter-connects that would replace regular electronic and optical inter-connects in electronic chips. [6, 7, 8].

Another research direction focuses on the quantum mechanical nature of plasmons. Experiments are aimed to measure the entanglement of photons mediated by plasmons [9]. Other experiment attempt to measure plasmon amplification by stimulated emission of excited molecules or atoms [10, 11, 12]. We would now turn to a theoretical overview for understanding the basis of these rich phenomena.

1.2 Electromagnetic Waves in Metals

The material properties of metals, like any other medium enter the Maxwell's equations through the complex dielectric function $\epsilon(\omega)$. The equation relevant for electromagnetic waves traveling inside a medium could be obtained by combining the two curl equations from Maxwell's equations giving:

$$\nabla \times \nabla \times \mathbf{E} + \epsilon(\omega)\frac{\omega^2}{c^2}\mathbf{E} = 0 \tag{1.1}$$

Using a plane wave basis in the form of $\mathbf{E} = \mathbf{E_0}e^{i(\mathbf{K}\cdot\mathbf{r}-\omega t)}$ this equation reduces to:

$$\mathbf{K}(\mathbf{K}\cdot\mathbf{E}) - K^2\mathbf{E} = -\epsilon(\omega)\frac{\omega^2}{c^2}\mathbf{E} \tag{1.2}$$

A general electromagnetic wave could be decomposed into a transverse wave and longitudinal wave. For transverse waves, for which the electric field is perpendicular to the propagation direction ($\mathbf{E} \perp K$), the term $\mathbf{K}\cdot\mathbf{E}$ equals to zero, and we get the dispersion relations in equation (1.3). This dispersion relation describes the wave properties traveling through the medium, and depends on the frequency dependent dielectric function $\epsilon(\omega)$:

$$K^2 = \epsilon(\omega)\frac{\omega^2}{c^2} \tag{1.3}$$

However, for longitudinal waves, for which the electric field is parallel to the propagation direction ($\mathbf{E} \parallel K$), the left side of (1.2) nullifies, implying that $\epsilon = 0$. For this configuration there are no traveling waves inside the metal, however collective oscillations where all the electrons in the metal move in phase, exist at frequencies for which ϵ vanishes. As implied by the longitudinal character of these modes, they could be excited only by longitudinal probes like fast electrons.

1.2.1 The Dielectric Function of Metals

For any material, all the optical processes including absorption/emission resonances and plasmon modes could be extracted from the dielectric function, $\epsilon(\omega)$. The response of metals could be described by a combination of two mechanisms which are the free electron response and inter-band transitions.

1.2.1.1 The Free Electron Response

The response of metals to an external electromagnetic field is dictated by the free electron movement of the conduction electrons. An external electric field creates a displacement of the free electrons from their equilibrium position which is associated with a dipole moment $\mu = e\mathbf{r}$ [4, 13]. The Sommerfeld model states that due to a strong electron-electron interaction all the electrons move in phase and create a macroscopic polarization $\mathbf{P} = n\mu$ in the material, where the displacement vector $\mathbf{D}$ is the sum of the external field and the induced polarization,

$$\mathbf{D}(\mathbf{r},t) = \epsilon_0\mathbf{E}(\mathbf{r},t) + \mathbf{P}(\mathbf{r},t) \tag{1.4}$$

The dielectric function ϵ relates the displacement $\mathbf{D}$ to the external field

$$\mathbf{D} = \epsilon_0\epsilon\mathbf{E} \tag{1.5}$$

By assuming a homogeneous medium the dielectric function can be expressed as

$$\epsilon = 1 + \frac{|\mathbf{P}|}{\epsilon_0|\mathbf{E}|} \quad . \tag{1.6}$$

The dielectric function in free electron metals can be obtained using the Drude model. By solving the equation of motion for a single free electron in the metal under an external harmonic field we can obtain the displacement of the electron from its equilibrium position,

$$m_e\frac{\partial^2\mathbf{r}}{\partial t^2} + m_e\gamma\frac{\partial\mathbf{r}}{\partial t} = eE_0e^{-i\omega t} \tag{1.7}$$

The equation of motion is solved by guessing a solution in the form of $\mathbf{r}(t) = \mathbf{r}_0 e^{-i\omega t}$ which gives a relation for the deviation from equilibrium as a function of the external field,

$$\mathbf{r}(t) = -\frac{e}{m(\omega^2 + i\gamma\omega)}\mathbf{E}(t) \tag{1.8}$$

.

For the polarization vector $\mathbf{P} = ne\mathbf{r}$ we get,

$$\mathbf{P} = -\frac{ne^2}{m_e(\omega^2 + i\gamma\omega)}\mathbf{E}(t) \tag{1.9}$$

and the dielectric function could be extracted by 1.6,

$$\epsilon(\omega) = \epsilon_1\omega) + i\epsilon_2(\omega) = 1 - \frac{\omega_p^2}{\omega^2 + \gamma^2} + i\frac{\omega_p^2\gamma}{\omega(\omega^2 + \gamma^2)} \tag{1.10}$$

where $\omega_p = \sqrt{\frac{ne^2}{\epsilon_0 m}}$ is the plasma frequency.

1.2.1.2 Inter-band Transitions

In addition to the free electron response of the conduction electrons, there is a contribution of inter-band transitions by the d band electrons in metals. For noble metals Ag and Au, these transitions occur at the visible range.

The inter-band transitions can be modeled using the Lorentz oscillator model where each transition has a distinct frequency and a certain width. Around that frequency there is a restoring force which is added to the above equation of motion 1.7 and gives,

$$m_e\frac{\partial^2\mathbf{r}}{\partial t^2} + m_e\gamma\frac{\partial\mathbf{r}}{\partial t} + \omega_0\mathbf{r}^2 = eE_0e^{-i\omega t} \quad . \tag{1.11}$$

This yields a solution for ϵ which has a lorentzian shape,

$$\epsilon_{interband} = 1 + \frac{\tilde{\omega}_p^2}{(\omega_0^2 - \omega^2) - i\gamma\omega} \tag{1.12}$$

Figure 1.1: Surface Plasmons at a Metal/Dielectric interface.

where here $\tilde{\omega}_p^2$ is the same expression as ω_p^2 but with $\tilde{n}$, the number of electrons associated with this transition.

The full dielectric response would therefore be a sum of the free electron response and the response due to inter-band transitions, $\epsilon = \epsilon_{drude} + \epsilon_{interband}$. If the excitation is off resonance with respect to the inter-band transition, the only contribution of the interband transition would be an overall addition of a constant to the real part of ϵ. This description fits the response of gold and silver very well [4].

1.2.2 Surface and Volume Plasmons

Since this work focuses on localized surface plasmons we would just briefly bring the results regarding the excitation of volume and surface plasmons.

For surface plasmons, following [14], let's look at the solution of equation (1.2) and of a similar equation for **H** for a configuration as depicted in Figure (1.1).

For a transverse wave ($\mathbf{K} \perp \mathbf{E}$) scattering off a plane in an arbitrary direction, it is convenient to work with the polarization base of transverse magnetic (TM) and transverse electric (TE) vectors. (For TM waves, the **H** vector resides inside the impact plane of the hitting wave with only E_x, E_z, H_y being nonzero and TE with **E** perpendicular to the impact plane, with only H_x, H_z, E_y being nonzero.)

Demanding the appropriate boundary conditions, continuity of $\mathbf{E} \parallel$and $\mathbf{H} \parallel$at the interface, yields two sets of solutions, one set for TM polarizations and the other for TE polarization.

For TM polarization the continuity of H_y and $D_z = \epsilon_i E_z$ (i=1,2 for the two half spaces)

yields,

$$\frac{k_2}{k_1} = -\frac{\epsilon_2}{\epsilon_1} \tag{1.13}$$

.

In addition, we require that H_y would fulfill the wave equation and get an additional condition on $k_1$and k_2:

$$k_1^2 = \beta^2 - k_0^2\epsilon_1 \tag{1.14}$$

$$k_2^2 = \beta^2 - k_0^2\epsilon_2 \tag{1.15}$$

Combining these three equations yields the dispersion relation for surface plasmon polaritons in terms of the propagation parameter β:

$$\beta = k_0\sqrt{\frac{\epsilon_1\epsilon_2}{\epsilon_1 + \epsilon_2}} \tag{1.16}$$

The dispersion curve of the excitations could be seen in figure 1.2.

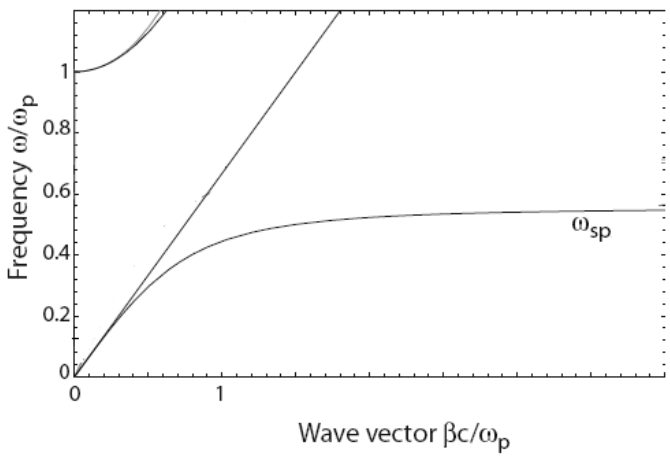

Figure 1.2: Dispersion relation for a Drude metal with negligible damping with a metal/dielectric interface. The curve has two distinct regimes: Bulk plasmons at $\omega > \omega_p$ and surface plasmon polaritons for $\omega < \frac{\omega_p}{\sqrt{2}}$

One can see that it is separated into two regions, the high frequency region for volume plasmons and the low frequency region for surface plasmons. By inserting the dielectric function obtained by the Drude model to the dispersion relation of propagating waves in equation (1.3) we get the following dispersion relation for volume plasmons.

$$\omega^2 = \omega_p^2 + K^2 c^2 \tag{1.17}$$

- For $\omega \geqslant \omega_p$, propagation of transverse electromagnetic waves into the bulk metal is allowed, supported by the oscillations of the metal conduction electrons in phase with the driving field. For most metals this regime occurs at the UV frequencies. In the case of $\omega = \omega_p$, ϵ vanishes and gives rise to a collective longitudinal mode where all the electrons move in phase. In fact there is a whole class of collective longitudinal modes, volume plasmons, for which ϵ vanishes and do not cross the light line and therefore could not be excited by light. These modes can be excited by longitudinal probes like fast moving electrons. For further reading on volume plasmons please refer to [15, 16].

- Above the horizontal asymptote, in the region of $\frac{\omega_p}{\sqrt{2}} < \omega < \omega_p$, the field inside the metal is decaying exponentially, hence, excitations do not propagate inside the metal. In this region the metal is reflective.

- The region of $\omega < \frac{\omega_p}{\sqrt{2}}$ (below horizontal asymptote in (1.2)) is the region of excitation of surface plasmons. At high k values the dispersion relation asymptotically reaches $\frac{\omega_p}{\sqrt{2}}$ and the group velocity $v_g = \frac{\partial \omega}{\partial q} = 0$ so the excitation has an electrostatic nature. For small k values (near the origin of (1.2)) the surface plasmons has a linear dispersion $\omega_{spp} = \frac{c}{\sqrt{\epsilon}}k < ck$, and do not cross the light line, hence, could not be excited regularly by optical means. In certain configurations, whether trough coupling the surface to a grating or a substrate with a higher dielectric constant, the lack of momentum is compensated and surface plasmon polaritons could be excited. For real metals, due to significant damping, these excitations can propagate along the surface only for a relatively short distance of a few microns. These modes are confined to the surface of the metal and do not propagate into the bulk.

1.3 Localized Surface Plasmon Resonance

Localizes Surface Plasmons Resonances (LSPR) are non-propagating excitations of the conduction electrons of metallic nano-structures coupled to the electromagnetic field. In contrast to the response of bulk metal to light at optical frequencies, in nanoparticles with size comparable to the skin depth, light induces a polarization which creates a restoring force on the electrons, giving rise to a resonance. In such a case, equation (1.7) would become an equation of a damped oscillator (Lorentz oscillator).

The localized plasmon resonance modes arise naturally from the solution of the scattering problem of a small, sub-wavelength dielectric nanoparticle in an oscillating electromagnetic field, first solved by Gustav Mie in 1908 [2].

1.3.1 Mie Theory

It is common to express the optical properties in terms of absorption and scattering cross sections σ_{abs} and σ_{sca}, or the total extinction cross section $\sigma_{ext} = \sigma_{abs} + \sigma_{sca}$. These cross sections are related to the loss of intensity of a parallel beam due to absorption or scattering as stated by the Beer-Lambert law:

$$\Delta I_{ext} = I_0(1 - e^{-N\sigma_{ext}z}) \tag{1.18}$$

Mie solved the problem of light scattering off spherical particles by the use of normal modes expansion of an incident plane wave in the base of vector spherical harmonics. The energy lost to scattering and absorption is obtained by integration of the different components of the Poynting vector across a sphere surrounding the particle. The extinction cross-section are calculated as a ratio of the total energy lost to absorption and scattering to the incident energy density.

The solution [4] is represented as a sum of amplitudes of different spherical modes of the sphere.

$$\sigma_{ext} = \frac{W_{abs} + W_{sca}}{I_{incident}} = \frac{2\pi}{|\mathbf{k}|^2} \sum_{l=1}^{\infty} (2l+1) Re[a_l + b_l] \quad , \tag{1.19}$$

where

$$a_l = \frac{m\psi_l(mx)\psi_l'(x) - \psi_l'(mx)\psi_l(x)}{m\psi_l(mx)\eta_l'(x) - \psi_l'(mx)\eta_l(x)} \tag{1.20}$$

$$b_l = \frac{m\psi(mx)\psi_l'(x) - m\psi_l'(mx)\psi_l(x)}{m\psi_l(mx)\eta_l'(x) - m\psi_l'(mx)\eta_l(x)} \quad . \tag{1.21}$$

The function ψ_l and η_l are Riccati-Bessel cylindrical function with $m = \frac{n(\omega)}{n_m}$, the ratio of the refractive index in the metal and the medium, and $x = |\mathbf{k}|a$, the size parameter. There is a resonance condition for these different plasmon modes.

Solution for the extinction coefficient, the ratio between the extinction cross-section and the physical cross-section of the NP, could be seen in Figure 1.3 for different NP diameters.

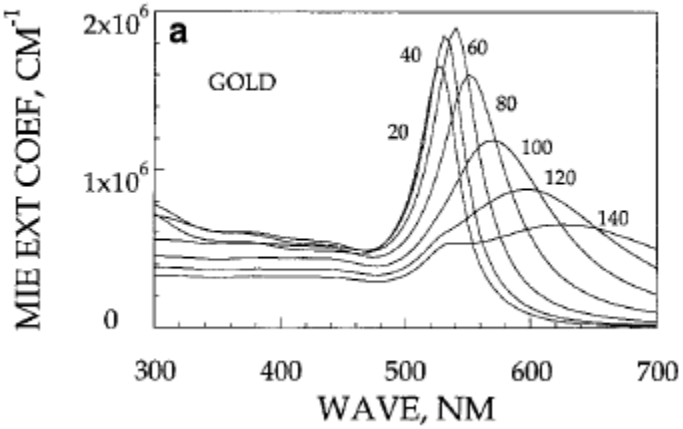

Figure 1.3: Mie extinction spectra for different sizes of gold NPs. Yguerabide and Yguerabide [17]

It is seen that the dipole plasmon mode redshifts as a function of the NP diameter. In addition, for particles larger than 100 nm a second peak could be seen which manifests an excitation of the quadruple plasmon mode which overlaps the dipole mode. The size dependence of the spectra originates from the retardation of the field, as for larger particles with sizes comparable to the wavelength of light in vacuum, different areas of the NP experience an electromagnetic field of different phases.

Another important implication of the Mie solution is the difference between the absorption and scattering cross-sections. The scattering peak position is redshifted with respect to the absorption peak. This fact influences the absorption and emission characteristics of exciton coupled to these plasmon modes.

1.3.1.1 The NP Shape Effect

Deviation from spherical symmetry has a large effect on the LSP line. An example for the shape dependence could be seen in Fig. 1.4 for the case of ellipsoid NPs. The dipole plasmon mode of ellipsoid NPs redshift as a function of their aspect ratio.

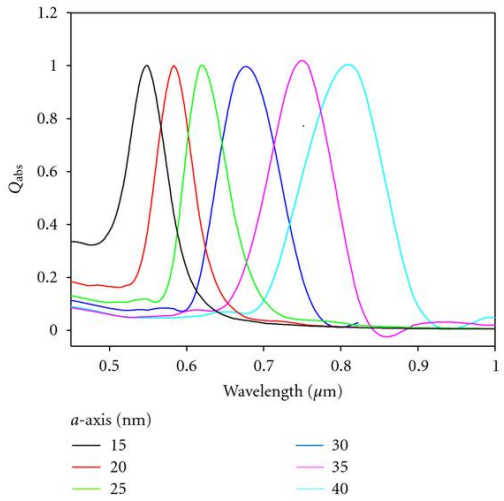

Figure 1.4: Extinction spectra of gold ellipsoid for different a axis (b=10 nm, c=5 nm Alsawafta et al. [18])

1.3.2 Normal Modes of a Polarizable Sphere

Although the Mie solution to the problem is accurate, it is still very instructive to examine the solution in the quasi-static limit as it will give us insight on the effects of plasmons on QD emission.

The quasi-static approximation ($\mathbf{K} \cdot \mathbf{r} << \mathbf{1}$) states that for a geometry of a size much less than the wavelength of light all the spatial points in the geometry, experience an external field with a negligible phase difference between them (no retardation of the field). This is equivalent to a solution of a static electric field, and the time dependence is obtained by adding a harmonic phase, $e^{-i\omega t}$.

This work concentrates on plasmons in nanoparticles with sizes less then 100 nm. In the visible range, the quasi-static treatment of the problem is a good approximation for this NP size range. Unlike in the Mie solution to the problem, in the quasi-static limit there is no size dependence of the spectra and it depends only on the frequency dependent ϵ.

The normal modes of the sphere arise in the solution of a charge free and current

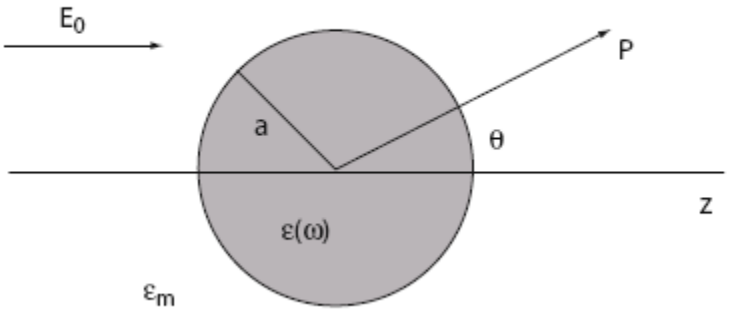

Figure 1.5: A sketch of a homogeneous sphere under an external field embedded in a medium with ϵ_m.

free Maxwell equation with boundary conditions at the sphere surface:

$$\nabla \cdot \mathbf{D} = \nabla \cdot (\epsilon(r,\omega)\mathbf{E}(r)) = 0 \quad . \tag{1.22}$$

The solution for equation (1.22) for a metallic sphere with a dielectric function $\epsilon(\omega)$ and an external medium having a real dielectric constant $\epsilon_m$will give the normal modes of the problem.

Assuming a homogeneous metal we have,

$$\epsilon(r,\omega) = \begin{cases} \epsilon_1(\omega) & r < a \\ \epsilon_m & r \geq a \end{cases} .$$

By defining $\mathbf{E} = \nabla\phi$, and because of the homogeneity of ϵ in each region, Equation 1.22 reduces to the Laplace equation:

$$\nabla \cdot (\epsilon(r,\omega)\mathbf{E}(r)) = \epsilon(\omega)\nabla \cdot \mathbf{E} = \epsilon(\omega)\nabla \cdot \nabla\phi = \epsilon(\omega)\nabla^2\phi = 0 \quad . \tag{1.23}$$

We solve the equation at the two spatial regions and get the solution:

$$\phi(r) = \begin{cases} Y_l^m r^l & r < a \\ \frac{Y_l^m}{r^{l+1}} a^{2l+1} & r \geq a \end{cases} . \tag{1.24}$$

The solutions to the problem is obtained by demanding that $\mathbf{D} \perp$to be continuous at the boundary:

$$\mathbf{D} \perp = \epsilon(r,\omega)\nabla\phi \quad \Longrightarrow \qquad \epsilon_1(\omega) l a^{l-1} Y_l^m = -\epsilon_m (l+1) a^{l-1} Y_m^l \tag{1.25}$$

which gives a constrain on the solution only to certain states, the eigen modes of the problem with l that satisfies,

$$\epsilon_1(\omega) = -\frac{l+1}{l}\epsilon_m \quad . \tag{1.26}$$

For each l of the different multipole orders, depending on the dielectric function of the material ϵ, there is a frequency that satisfies this condition. It will be shown later that at these frequencies there is an excitation of plasmon modes where the local electric field is resonantly enhanced.

1.3.3 Plasmon Mode Excitations

In the last section we have solved the problem of a sphere with a zero external potential and obtained the eigen modes of the sphere. We will now discuss the excitation of these modes by an external field. An external field excitation is introduced by applying an external potential as a boundary condition to the Laplace equation. In our treatment we would relate to two cases: plane wave excitation and excitation by a local dipole in the vicinity of the metallic sphere.

1.3.3.1 Plane Wave Excitation

A plane wave with the electric field pointing at the Z direction, corresponds in the quasi-static limit to a uniform field along the Z direction. This field is introduced as a boundary condition to the Laplace equation by defining an external potential of the form $\phi_{out} = -E_0 z = -E_0 r\cos\theta$ as $r \longrightarrow \infty$.

A general solution to Equation (1.23) is a sum of the set of functions given in (1.24). Neglecting the phase given by the $e^{im\phi}$ of the spherical harmonics we have the following solutions for the potential inside and outside of the sphere:

$$\phi_{in}(r,\theta) = \sum_{l=0}^{\infty} A_l r^l P_l(\cos\theta) \tag{1.27}$$

$$\phi_{out}(r,\theta) = \sum_{l=0}^{\infty} [B_l r^l + C_l \frac{1}{r^{l+1}}] P_l(\cos\theta) \tag{1.28}$$

By imposing the boundary conditions at $r = a$, and at $r \longrightarrow \infty$ only the $l = 1$ solution is non zero,

$$\phi_{in}(r,\theta) = -\frac{3\epsilon_m}{\epsilon(\omega) + 2\epsilon_m} E_0 r \cos\theta \tag{1.29}$$

$$\phi_{out}(r,\theta) = -E_0 r\cos\theta + \frac{\epsilon(\omega) - \epsilon_m}{\epsilon(\omega) + 2\epsilon_m} E_o a^3 \frac{\cos\theta}{r^2} \quad . \tag{1.30}$$

The solution outside the sphere could be rewritten as a potential of a dipole:

$$\phi_{out}(r,\theta) = -E_0 r\cos\theta + \frac{\mathbf{p}\cdot\mathbf{r}}{4\pi\epsilon_0\epsilon_m r^3} \tag{1.31}$$

where

$$\mathbf{p} = 4\pi\epsilon_0\epsilon_m a^3 \frac{\epsilon - \epsilon_m}{\epsilon + 2\epsilon_m}\mathbf{E_0} \quad . \tag{1.32}$$

In this case the electric field outside the sphere looks like a superposition of the external field and the field of a dipole located at the origin:

$$\mathbf{E}_{out} = \mathbf{E}_0 + \frac{3\mathbf{n}(\mathbf{n}\cdot\mathbf{p} - \mathbf{p})}{4\pi\epsilon_0\epsilon_m}\frac{1}{r^3} \quad . \tag{1.33}$$

The dipole $\mathbf{p}$ is resonantly enhanced at $\epsilon(\omega) = -2\epsilon_m$ which is the resonance condition obtained at (1.26) for the dipole mode with $l = 1$. This condition could be satisfied for metals, where the real part of the dielectric function is negative for a wide band of frequencies.

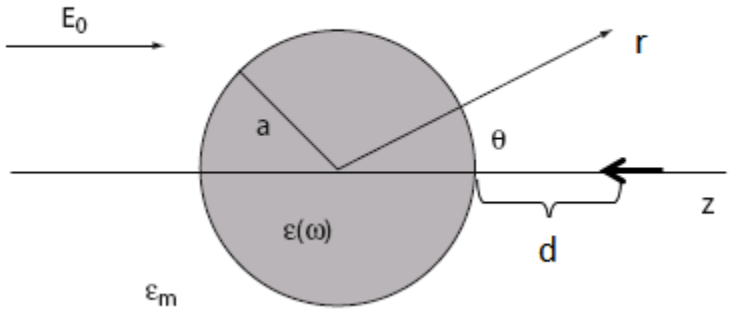

Figure 1.6: A dipole placed near a sphere of radius a with a distance d from its surface.

1.3.3.2 Excitation of Plasmons in a Sphere by a Local Dipole

As we have seen in (1.24) the solutions outside and inside the sphere are:

$$\phi_{out}(\mathbf{r}) = \sum_{l=0}^{\infty} C_l \frac{P_l(\cos\theta)}{r^{l+1}} \tag{1.34}$$

$$\phi_{in}(\mathbf{r}) = \sum_{l=0}^{\infty} A_l r^l P_l(\cos\theta) \quad . \tag{1.35}$$

Let us now introduce a potential which corresponds to a dipole situated outside the sphere. By applying the boundary conditions, continuity of the potential and its derivative, we can solve for the total potential outside the sphere as a superposition of two potential:

$$\phi_{out} + \phi_{dipole} = \phi_{in} \qquad for\ r = a \tag{1.36}$$

and

$$\epsilon_m \frac{\partial}{\partial r}(\phi_{out} + \phi_{dipole}) = \epsilon_1 \frac{\partial}{\partial r}\phi_{in} \qquad for\ r = a \quad . \tag{1.37}$$

An illustration of the problem could be seen in Figure 1.6.

On the other hand, we express the potential that originates from a dipole of size μ placed on the z axis at a distance d from the surface by the following multipole expansion :

$$\phi_{dipole}(\mathbf{r}) = \frac{\mu}{4\pi\epsilon_0}\sum_{l=0}^{\infty}\frac{(l+1)r^l}{(a+d)^{l+2}}P_l(\cos\theta) \tag{1.38}$$

The solution of the potential outside the sphere is obtained by applying the above boundary conditions and finding C_l and A_l (1.35). The resulting potential outside the sphere is :

$$\phi_{out}(\mathbf{r}) = -\frac{\mu}{4\pi\epsilon_0}\sum_{l=0}^{\infty}(l+1)\times\frac{\epsilon_1(\omega)-\epsilon_m}{\epsilon_1(\omega)+\frac{l+1}{l}\epsilon_m}\times\frac{a^{2l+1}}{(a+d)^{l+2}}\times\frac{P_l(\cos\theta)}{r^{l+1}} \quad . \tag{1.39}$$

This result resembles the structure of a multipolar expansion of a potential. The different terms are the multipolar orders with frequency and size dependence coefficients . We could define a multipolar polarizability as the frequency dependent part of the multipolar coefficient:

$$\alpha_l \equiv \frac{\epsilon_1(\omega)-\epsilon_m}{\epsilon_1(\omega)+\frac{l+1}{l}\epsilon_m} \quad . \tag{1.40}$$

For frequencies satisfying the condition we obtained at (1.26), $\epsilon_1(\omega) = -\frac{l+1}{l}\epsilon_m$, the multipole of order l is resonantly enhanced and corresponds to a plasmon resonance in the metal.

From this result we could understand the frequency dependent resonant behavior of the problem (leaving the distance dependence for a detailed discussion in the next section.) A local dipole oscillating with a frequency ω, excites a whole set of plasmon modes depending on the spectral overlap with the different frequency dependent plasmon modes described by α_l. Coupling of the dipole inside a QD to different plasmon modes results in quenching or enhancement of the light emitted to the far field depending on the plasmon mode order. In a similar fashion to what we have seen for the case of plane wave excitation, only the dipole plasmon mode can couple to the far field. Hence, an overlap with a high order l mode results in quenching of the luminescence

while an overlap with the dipole mode results in enhanced radiative rate since both the molecular and the plasmonic dipoles contribute to light emission.

1.4 Exciton-Plasmon Interactions

With most of the concepts laid out in the previous sections we could now have a more complete description of the interactions of QDs and metal NPs illuminated by light. By assuming a field which is spatially varying slower than a size of a QD we could represent its optical response by that of a point dipole. This is indeed the case for a QD with a distance of a few nanometers from a NP.

Our goal is to calculate the magnitude of a dipole μ located at $\mathbf{r_0}$, induced by the cumulative response of external light and the nearby metal NP. We will demonstrate the change in the QD emission by comparing the emission properties of this induced dipole to the case of an illuminated QD without the presence of a metal NP.

1.4.1 The Drude Lorentz Model for Molecular Emission

We have introduced the Drude Lorentz model in 1.11 for the interband transitions in metals. In fact this model is commonly used to describe molecular emission.

Multiplying equation 1.11 by e, the charge of an electron, and defining $\mu = er$ we get the equation of motion for the dipole:

$$\ddot{\mu} + \Gamma_0 \dot{\mu} + \omega_0^2 \mu = (\frac{e^2}{m}) \overleftrightarrow{f} \cdot \mathbf{E}(\mathbf{r}, t) \tag{1.41}$$

Generally, the QD or molecule does not have to be isotropic, hence μ does not have the same orientation as the exciting field $\mathbf{E}$. This is represented by $\overleftrightarrow{f}$, the oscillator strength, which is a tensor that incorporates the different contributions of the different molecular axes, and its magnitude corresponds to the absorption rate.

Having $\mathbf{E}(\mathbf{r}, t) = e^{-i\omega t}\mathbf{E}(\mathbf{r}, \omega)$ and, in the quasi-static limit, $\mathbf{E}(\mathbf{r}, \omega) = \mathbf{E}(\omega)$ we obtain a solution for μ:

$$\mu(\omega) = \frac{\frac{e^2}{m}\overleftrightarrow{f}\cdot\mathbf{E}(\omega)}{\omega_0^2 - \omega^2 - i\omega\Gamma_0} = \overleftrightarrow{\alpha}(\omega)\cdot\mathbf{E}(\omega) \tag{1.42}$$

where $\overleftrightarrow{\alpha}(\omega)$ is the frequency dependent polarizability, ω_0 and Γ_0, the emission line center and linewidth.

With this solution we could derive the extinction coefficient, the energy lost from an incident beam due to scattering an absorbance. For the isotropic case, the extinction coefficient has a lorentzian shape:

$$K = \frac{\frac{\Gamma_0}{4c}\frac{fe^2}{m}}{(\omega_0 - \omega)^2 + (\frac{\Gamma_0}{2})^2} \tag{1.43}$$

In a relaxation experiment, where we turn off the excitation $\mathbf{E}(\omega)$, we obtain:

$$\mu(t) = \mu_0 e^{-i\omega_0 t} e^{-\frac{\Gamma_0}{2}t} \tag{1.44}$$

and see that $\frac{1}{\Gamma_0}$ is the excited state lifetime.

1.4.2 The effects of Plasmon-Exciton Interactions on QD Emission

Following [19] the local field that generates an induced dipole in the QD is a sum of incident field, the field reflected by the metal NP at the position of the dipole, and an image field created by the dipole itself,

$$\mathbf{E}_{local}(\mathbf{r_0}, t) = \mathbf{E}_{incident}(\omega) + \mathbf{E}_{reflected}(r_0;\omega) + \mathbf{E}_{image}(r_o, r_0;\omega) \quad . \tag{1.45}$$

The reflected and the image fields are resonantly enhanced at frequencies around the plasmon resonance.

1.4.2.1 The Dyadics $\overleftrightarrow{G}(r, r_o;\omega)$ and $\overleftrightarrow{R}(\mathbf{r_0};\omega)$

In the case of an harmonic time dependence for the oscillating dipole $\mu(t) = \mu(\omega)e^{-i\omega t}$, it is useful to define the dyadic Green's function which relates the electric field $\mathbf{E}(r,\omega)$ in the point $\mathbf{r}$ in space to a source dipole located at $\mathbf{r_0}$ [19]:

$$\mathbf{E}(\mathbf{r},\omega) = \overleftrightarrow{G}(\mathbf{r},\mathbf{r_0};\omega)\cdot\mu(\omega) \quad . \tag{1.46}$$

The dyad $\overleftrightarrow{G}$ could be represented as the sum of the free dipole contribution and the contribution of the presence of the metallic NP, as $\mathbf{E}(\mathbf{r},\omega) = [\overleftrightarrow{G_0}(\mathbf{r},\mathbf{r_0};\omega) + \overleftrightarrow{G_{metal}}(\mathbf{r},\mathbf{r_0};\omega)]\cdot\mu(\omega)$.

The quantity $\overleftrightarrow{G_{metal}}$ contains all the effects of the metal on the dipole radiation.

It is also useful to define the reflection dyad $\overleftrightarrow{R}(\mathbf{r_0};\omega)$ which relates the incident field to the local field at the dipole position created by the polarization of the metal NP,

$$\mathbf{E}_{reflected}(\mathbf{r_0};\omega) = \overleftrightarrow{R}(\mathbf{r_0};\omega)\cdot\mathbf{E}_{incident}(\omega) \quad . \tag{1.47}$$

1.4.2.2 The Modification of Spontaneous Emission

Having set up all the relevant concepts we could now turn to examine the change in spontaneous emission of a dipole μ by the presence of a metal NP.

For the local field that creates the driving force (1.45), we substitute the relevant expressions using the appropriate dyadics:

$$\mathbf{E}(\mathbf{r_0},\omega) = [\overleftrightarrow{\mathbf{I}} + \overleftrightarrow{\mathbf{R}}(\mathbf{r}_0;\omega)]\cdot\mathbf{E}_{incident}(\omega) + \overleftrightarrow{\mathbf{G}_{metal}}(\mathbf{r_0},\mathbf{r_0};\omega)\cdot\mu(\omega) \quad . \tag{1.48}$$

With this expression for the driving field we could solve the equation of motion for μ (1.41) with the ansatz $\mu(\omega,t) = \mu(\omega)e^{-i\omega t}$:

$$-\omega^2\mu(\omega)+\omega_0^2\mu(\omega)-i\omega\Gamma_0 = \frac{e^2}{m}\overleftrightarrow{\mathbf{f}}\cdot\{[\overleftrightarrow{\mathbf{I}}+\overleftrightarrow{\mathbf{R}}(\mathbf{r_o};\omega)]\cdot\mathbf{E}_{incident}(\omega)+\overleftrightarrow{\mathbf{G}_{metal}}(\mathbf{r_0},\mathbf{r_0};\omega)\cdot\mu(\omega)\} \quad . \tag{1.49}$$

It is instructive to examine a simplified case where μ is aligned along the $\hat{z}$ and $\overleftrightarrow{\mathbf{G}} = G\hat{z}\hat{z}$. By separating $\overleftrightarrow{\mathbf{G}_{metal}} = Re[\overleftrightarrow{\mathbf{G}_{metal}}] + Im[\overleftrightarrow{\mathbf{G}_{metal}}]$ and rearranging the terms in (1.49) we obtain the same structure of equation (1.42) for the uncoupled dipole emission but with a modified lorentzian lineshape:

$$\mu(\omega) = \frac{1}{\omega^2-\omega_0^2-\Delta^2(\omega)-i\omega\Gamma_{eff}} \times \frac{e^2}{m}\overleftrightarrow{f_{eff}}\cdot\mathbf{E}_{incident} \tag{1.50}$$

with :

$$\overleftrightarrow{f_{eff}} = \overleftrightarrow{\mathbf{f}} \cdot [\overleftrightarrow{\mathbf{I}} + \overleftrightarrow{\mathbf{R}}(\mathbf{r_o};\omega)] \quad (1.51)$$

$$\Gamma_{eff} = \Gamma_0 + \frac{e^2}{m}|f|Im[\overleftrightarrow{\mathbf{G}_{metal}}(\mathbf{r_0},\mathbf{r_0};\omega)] \quad (1.52)$$

$$\Delta^2(\omega) = \frac{e^2}{m}|f|Re[\overleftrightarrow{\mathbf{G}_{metal}}(\mathbf{r_0},\mathbf{r_0};\omega)] \quad (1.53)$$

- Δ^2 represents a shift in the lineshape peak, and is negligible at optical frequencies.
- $\overleftrightarrow{f_{eff}}$ is the effective oscillator strength; it is enhanced by the presence of the metal by a factor which, is the local field enhancement. A large oscillator strength corresponds to an enhanced absorption rate of the QD, and depends on the spectral overlap of the dipole absorption line and plasmon resonances in the metal NP .
- The effective linewidth Γ_{eff} is larger than the intrinsic linewidth Γ_0 and depends on the imaginary part of $\overleftrightarrow{\mathbf{G}_{metal}}(\mathbf{r_0},\mathbf{r_0};\omega)$. Therefore, in a relaxation experiment, as described above (1.44), we would have a faster damping of the dipole oscillations. This spectral broadening depends on the overlap of the dipole emission line with plasmon resonances in the metal NP.

1.4.2.3 Coupling of a Dipole to a Metal Sphere

Having the results for the electric field for plane wave excitation and for a local dipole excitation we could put all the parts together for the interaction of a metal sphere with a local dipole (Figure 1.6). By solving for Γ_{eff} and for $\overleftrightarrow{f_{eff}}$ we will see the spectral and spatial dependence of the coupling of the dipole to different plasmon modes.

The local field as obtained in section 1.3.3.1 at the location of the dipole $\mathbf{r_0} = (\mathrm{a}+\mathrm{d})\hat{\mathbf{z}}$ is:

$$\mathbf{E}_{reflected}(\mathbf{r_0}) = \overleftrightarrow{\mathbf{R}}(\mathbf{r_o};\omega)\cdot\mathbf{E}_{incident} = 2\times\frac{\epsilon(\omega)-\epsilon_m}{\epsilon(\omega)+2\epsilon_m}\times\frac{a^3}{(a+d)^3} \quad (1.54)$$

The effective oscillator strength is therefore:

$$\overleftrightarrow{f_{eff}} = \overleftrightarrow{\mathbf{f}} \cdot [\overleftrightarrow{\mathbf{I}} + \overleftrightarrow{\mathbf{R}}(\mathbf{r_o};\omega)] = f[1 + 2 \times \frac{\epsilon(\omega) - \epsilon_m}{\epsilon(\omega) + 2\epsilon_m} \times \frac{a^3}{(a+d)^3}] \tag{1.55}$$

We will now obtain an expression for Γ_{eff}.

Using the results of section 1.3.3.2 the image field at $\mathbf{r_0}$ created by the dipole due to the dipole itself is:

$$\mathbf{E}_{inage} = \overleftrightarrow{\mathbf{G}_{metal}}(\mathbf{r_0}, \mathbf{r_0};\omega)\mu(t) = \mu(t)\sum_{l=1}^{\infty}(l+1)^2 \times \frac{\epsilon(\omega) - \epsilon_m}{\epsilon(\omega) + \frac{l+1}{l}\epsilon_m} \times \frac{(\frac{a}{a+d})^{2l+1}}{(a+d)^3} \quad . \tag{1.56}$$

Substituting $\overleftrightarrow{\mathbf{G}_{metal}}(\mathbf{r_0}, \mathbf{r_0};\omega)$ in the expression for Γ_{eff} we could readily get the total decay rate :

$$\Gamma_{eff} = \frac{e^2}{m}|f|im[\overleftrightarrow{\mathbf{G}_{metal}}(\mathbf{r_0}, \mathbf{r_0};\omega)] = \Gamma_0 + \frac{e^2}{m}|f|\sum_{l=1}^{\infty}(l+1)^2 \times Im[\frac{\epsilon(\omega) - \epsilon_m}{\epsilon(\omega) + \frac{l+1}{l}\epsilon_m}] \times \frac{(\frac{a}{a+d})^{2l+1}}{(a+d)^3} \quad . \tag{1.57}$$

With this analytical solution we could get an insight into the effect of the metal on the absorption and emission of the dipole. The effective oscillator strength $\overleftrightarrow{f_{eff}}$ manifests the change in the absorption rate of the dipole. It scales as $\frac{a^3}{(a+d)^3}$ and is resonantly enhanced at the dipole plasmon mode where $\epsilon(\omega) = -2\epsilon_m$.

The total decay rate Γ_{eff} is a sum of radiative decay and of non radiative decay rates. It is proportional to the imaginary part of $\overleftrightarrow{\mathbf{G}_{metal}}(\mathbf{r_0}, \mathbf{r_0};\omega)$ and could be separated into the different multipole plasmon modes. As we have seen, in the quasi-static limit only the dipole plasmon mode can radiate and therefore contribute to the radiative decay of the dipole. The higher multipole modes could not radiate; some of the energy is stored in the near field and could be reabsorbed in the dipole and the rest dissipates into heat.

In this model we could examine the distance dependence of the excitation of the different plasmon modes. For the resonance condition of the different multipoles, $\epsilon(\omega) = -\frac{l+1}{l}\epsilon_m$, we can get a simplification of the frequency dependent part of Γ_{eff},

$$Im[\frac{\epsilon(\omega) - \epsilon_m}{\epsilon(\omega) + \frac{l+1}{l}\epsilon_m}] = \frac{(2l+1)\epsilon_m}{l \times Im[\epsilon(\omega)]} \quad . \tag{1.58}$$

l\d	**0.1 [nm]**	**1 [nm]**	**5 [nm]**	**10 [nm]**	**15 [nm]**
1	4.35	4	1.76	0.79	0.39
2	8	6	2.42	0.83	0.32
3	13	10	2.96	0.78	0.24
4	20	14	3.27	0.66	0.16
5	28	19	3.38	0.52	0.1
10	87	42.8	2.2	0.094	0.059
50	1300	64.2	2.12×10^{-4}		
100	–	9.4			
200	–	0.053			
1000	940				
2000	5				
5000	6.4×10^{-8}				

Table 1.1: The different multipole contribution, $I_l \times 10^{-7}$ to the modified decay rate Γ_{eff} as a function of the distance from the NP surface, d [nm]. Adopted from Metiu [19].

Inserting (1.58) into (1.57) we can factor out an expression for the weight of the different multipolar orders in the expansion of the decay rate:

$$I_l \equiv (l+1)^2 \frac{2l+1}{l} \frac{(\frac{a}{a+d})^{2l+1}}{(a+d)^3} \quad . \tag{1.59}$$

It is evident that at very short distance from the surface most of the total decay rate comes from excitation of high order plasmon modes, which results in dissipation into heat. At larger distances more weight is given to the dipole mode, hence, more of the energy will result in emission of light.

As for the oscillator strength, $\overleftrightarrow{f}$, the local field enhancement decreases with the distance from the surface as $\frac{a^3}{(a+d)^3}$. Therefore, we can see there is a trade off between the local field enhancement that decreases with the distance and the emission efficiency that increases with the distance. For having the maximal emission efficiency we would choose an optimal distance that maximizes these two quantities.

1.5 The Scope of this Work

We could summarize the effect of a metal NP on QD emission in the following contributions:

- The absorption of light in QDs is increased due to the local field enhancement upon plasmon excitation. The enhancement depends on the overlap of the QD absorption band and the dipole plasmon resonance and decrease like $\frac{a^3}{(a+d)^3}$ as a function of the distance from the surface.

- The total decay rate of excitons in QDs is enhanced due to energy transfer to metal NP plasmon modes. The rate of the energy transfer to the different modes depends on the QD-metal NP separation and on the spectral overlap between the QD emission and the different plasmon mode.

- The energy transfer to the metal NP could result in emission enhancement or quenching due to coupling to different order plasmon modes: Efficient coupling to the dipole plasmon mode at the expense of the other modes would result in emission enhancement like the effect of an antenna, where the image dipole created in the metal NP contributes to the emission. Coupling to higher order modes will results in loss into heat, as radiation from these modes does not propagate into the far field.

- There is an optimal QD-NP separation for which the total light emission is maximal. It is a trade off between the absorption rate which decreases with the distance and the emission rate which increases with the distance.

- In cases for which the energy transfer rate is larger than the plasmonic decay rate, a gain of surface plasmons could be achieved that would cause a narrowing of the resonant mode in a manner similar to that of a laser. [10, 12, 11]

The theory in this field is well established and gives quantitative predictions to the local field enhancements and to the lifetime shortening, however, there is quite a large

variation in published experimental results. Experiments measuring fluorescence of molecules or QDs near metal NPs show a broad range of enhancement values, between 2 and 20, [20, 21, 22, 23, 24, 25, 26, 27] depending on the metal and the molecule types. On the other hand, other experiments show that there is a partial or total quenching of the emission intensity[28]. There are several studies that measure the distance dependence of this effect indicating that there is an optimal distance for the enhancement, but it changes from one system to another [21, 29].

The ambiguity in the experimental findings can be traced to both synthesis difficulties and to measurement problems. The synthesis challenge is to produce well defined structures, in which both the plasmon resonance local field profile and the QD-NP separation is precisely controlled and verified. This cannot be achieved when using organic molecules, which cannot be observed in electron microscopy. Furthermore, more complex structures are even harder to produce in a reproducible manner.

The measurement challenge is the ability to separate between the different mechanisms which constitute the exciton-plasmon interaction. Most experiments focus on measuring the emission only, which we showed above , is given by a product of the absorbed power and the emission rate. Hence, these simplistic measurements fail to properly describe the various processes involved.

In this work we address both challenges:

We have developed reproducible methods for the synthesis of gold NPs by wet chemistry as well as by e-beam lithography. Using DNA and protein based self-assembly as well as top down methods, these NPs are assembled into structures together with semiconductor QDs. These QDs are observable in TEM and let us determine the number of QDs and the QD-NP separation in our structures.

Rather than measuring the simple emission spectra we conduct photoluminescence excitation measurements (PLE) and polarization dependent measurements on a single nanostructure level. Using these methods we are able to directly measure and control the absorption rate enhancement of QD-NP structures apart from direct measurements of the increase in the exciton decay rate.

Chapter 2

Methods

In this chapter we survey the methods used in this work. We start with gold NP synthesis and continue with the methods for self-assembly of NP-QD structures. Subsequently we describe the different optical measurement methods we have used in this work for measuring the absorption enhancement and the lifetime modification. We end with a description of the methods used to measure the emission and polarization dependence of single objects.

2.1 Synthesis Protocols

2.1.1 17 nm Gold NP Synthesis:

A 20 ml solution of 0.2% w/v $Na_3 - Citrate$ + 25 µl of 1% w/v Tannic Acid heated to 60 ^0C is added under vigorous stirring to a solution which consists of 1 ml of 1% w/v $NaAuCl_4$ diluted to 80 ml DI water. The solution is heated to boil and is then boiled for another 10 minutes and cooled to room temperature. (All reagents by Sigma)

2.1.2 80 nm Gold NP synthesis:

1ml of 17 nm gold NP solution is put in a 50 ml plastic falcon tube.

1. 1 ml of 0.01% $NaAuCl_4$ is added under stirring on vortex.
2. Sequentially 40 µl of 40 mM hydroxyl-amine is added under vigorous stirring.
3. Steps 1-2 are repeated until a volume of 10 ml is reached.
4. The NP solution is transferred to an erlenmeyer, heated to boil, boiled for 10 min and cooled to room temperature.
5. Steps 1-2 are repeated until a volume of 100 ml is reached, on a magnetic stirrer.
6. BSPP (bis-P-sulfonatophenylphosphine) (Sigma) is added to the solution with a final concentration of 93 mM and left overnight at room temperature.

2.1.3 QD-NP Conjugates Synthesis:

2.1.3.1 DNA Hybridization:

DNA Sequences:

- Sequence 1- 5'-biotin-GCAGTAACGC TATGTGACCG-3'-thiol
- Sequence 2- 5'-CGGTCACATA GCGTTACTGC-3'

dsDNA- Sequence 1, and Sequence 2 at a concentration of 0.5 mM are mixed in a 1:1 ratio, and reacted with TCEP (tris-carboxyethylphosphine) (Sigma) with a final concentration of 5 mM TCEP and stirred on vortex. The solution is left for at least 20 min for hybridization at room temperature and then diluted to 1 µM in DI water.

QD-DNA Conjugates: Streptavidin coated QD (Qdots Invitrogen) emitting at 565,585,605,655 and 705 nm, at a concentration of 1 µM are reacted with dsDNA at 1:1 ratio (for NP-QD conjugates) ratio and at 1:2 ratio (for NP-QD-NP conjugates).

Self Assembly of Gold NP-QD Structures:

1. For the assembly of structures having multiple QDs and a single gold NP, QD-DNA hybrids (1:1 QD:DNA) are added to 80 nm gold NP solution at 100:1 ratio at equal volumes. After overnight at room temperature the excess unreacted QD-DNAs are separated with 6 cycles of centrifugation and resuspension after removing the supernatant (600g at a benchtop centrifuge for 5 minutes.)

2. For the assembly of structures having a single QD attached to a single gold NP, QD-DNA hybrids (1:1 QD:DNA) are reacted with NPs at 1:1 ratio.

3. For the assembly of structures having a single QD attached between two gold NP, QD-DNA hybrids (1:2 QD:DNA) are reacted with NPs at 1:2 ratio.

Purification: The reaction products of are purified by gel electrophoresis using 1% agarose with a 1/2xTBE in a current of 40 mAmps. The desired fraction is cut from the gel and extracted using dialysis micro tubes (Geba-Flex microtubes dialysis kit). A small fraction of the products is examined by TEM.

2.1.4 Top Down Fabrication of QD-NP Structures

We have fabricated 80 nm hemispheres encapsulated with layers of QDs embedded in silica.

1. Two layers of PMMA resists of different viscosities are spin cast on a Si wafer with 150 μm oxide layer. A pattern of an array 80 nm diameter circles is implemented into the resist by a 100 KV electron beam using a JEOL E-Beam.

2. After the resist is developed, there is a 80 nm hole array in the resist with an under-cut. 7 nm Ti and 25 nm of Au are evaporated on the sample using an electron beam evaporator. The pitch of the array was around 500 nm, large enough for not having significant near-field coupling between neighboring NPs.

3. On the gold hemispheres we have assembled silica caps embedded with QDs. We make use of HSQ negative e-beam resist for making a 10 nm layer on top of the dots. On top of that layer we spin cast CdSe/ZnS QD layer and cover them with another layer of HSQ.

4. We expose the layered structure to a 100 kV electron beam, the HSQ hardens and form silica caps on top of the gold hemispheres having QDs embedded inside. The unexposed regions are washed off in development in a harsh basic environment.

2.2 Optical Measurement Schemes

In this section we present the different optical measurement methods used in this work; extinction spectroscopy, used for measuring the plasmon resonance of gold NPs in solution, photoluminescence excitation spectra and lifetime measurements of NP-QD structures in solution, and polarization dependent single object spectroscopy.

2.2.1 Plasmon Resonance Extinction Spectroscopy

The most straight forward way for characterizing the plasmon resonance of colloidal gold NPs in solution is by using extinction spectroscopy. We use an absorption UV-vis spectrophotometer. Monochromatic light illuminates the sample and a detector detects the amount of light that is transmitted through the sample in the forward direction. Light which is absorbed by the sample or is scattered in all directions does not pass forward to the detector. By scanning the incident light wavelength and performing this measurement we get the extinction (absorption+scattering) of the sample.

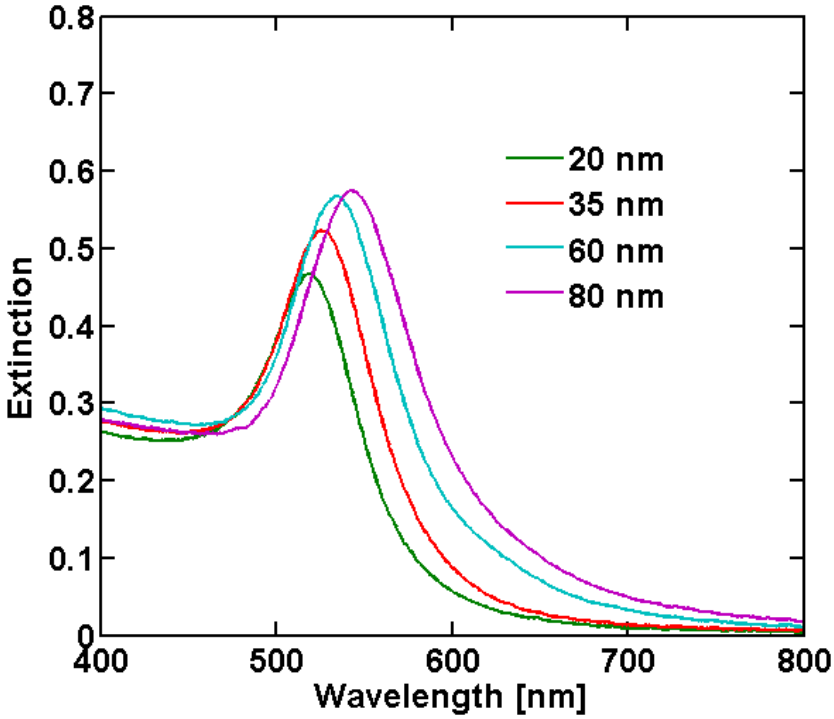

Figure 2.1: Extinction spectrum of gold NPs in aqueous solution.

2.2.2 Photoluminescence Excitation Spectra - PLE

A PLE measurement is conducted by tuning the excitation wavelength and detecting the respected changes in emission of the exciton resonance. This enables us to determine the absorption spectrum and separate the contribution due to absorption enhancement from the other mechanisms. As the excitation and emission are not at the same wavelength, the scattered light is filtered by the detection monochromator as seen in Figure 2.2.

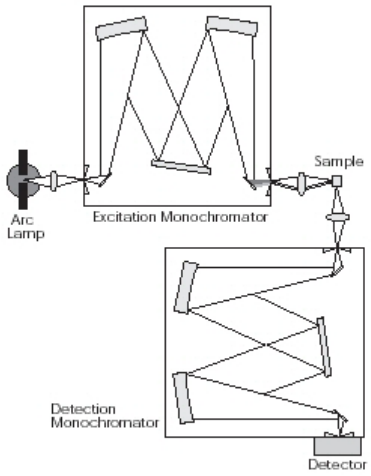

Figure 2.2: A fluorimeter apparatus.

The sample is put inside a cuvette, a transparent quartz tube. White light from an arc lamp enters the excitation monochromator and only a narrow band of frequencies is illuminated on the sample. Emitted light from the sample is collected at an angle of 90^o and is focused on the detection monochromator entrance slit. The light is detected by a PMT detector. This apparatus gives the ability to measure the emission spectrum of a sample as well as the excitation spectrum of the sample. We have used a Jobin-Yvon Fluorolog-3 apparatus for our measurements

2.2.3 Lifetime Measurements

Lifetime measurements were performed on aquaeous solutions of nanorstructures on a spectrofluorimeter with a pulsed LED excitation. The emission is collected by a time corelated single photon counting module (TCSPC).

2.2.4 Polarization Dependent Measurements

As implied from equations 1.33 and 1.32, the spatial distribution of light around the metal NP has a dipole shape, which is aligned along the incident light polarization.

Therefore, the QD would be effectively excited when it resides on a peak of that distribution, and conversely - when it resides on a node. We have installed a polarization rotator (Newport PR-550) in our micro epi-fluorescence microscope and controlled the rotation by a computer. This way we have measured the intensity of the QD emission as a function of the polarization angle. This measurement gives a quantitative measure of the local field enhancement factor.

2.3 Single NP Spectroscopy

In this section we describe the methods used for single NP-QD structure studies. Conducting quantitative studies of fluorescence from a single QD requires a good characterization of the illumination profile and the precise positioning of the QD in the center of the beam. The light level emitted from a single QD require efficient collection and measurement of light from the sample.

2.3.1 Tight Focus and Polarization Rotation in the Focal Spot.

Our measurement system includes an inverted microscope (Nikon Eclipse TE) with a X60 oil immersed objective with a large NA(1.4). Laser light of 532nm diode laser or 633 nm He-Ne laser enter the microscope and is reflected by a dichroic beam splitter and focused to a diffraction limit spot on a sample. Before entering the microscope the light is passed through a polarization rotator which give the ability of changing the exciting polarization.

The spot is characterized by fluorescent gel which gives a Gaussian shaped focus. This feature is important for two reasons. The first reason is the repeatable exciting intensity in order to compare the emission intensity of different samples and the second reasons is for polarization dependent experiments. The Gaussian shaped focus ensures a plane wave excitation at the focus which will give a polarization in the focal plane [13]. The Gaussian shape of the focus could be seen in Figure 2.3.

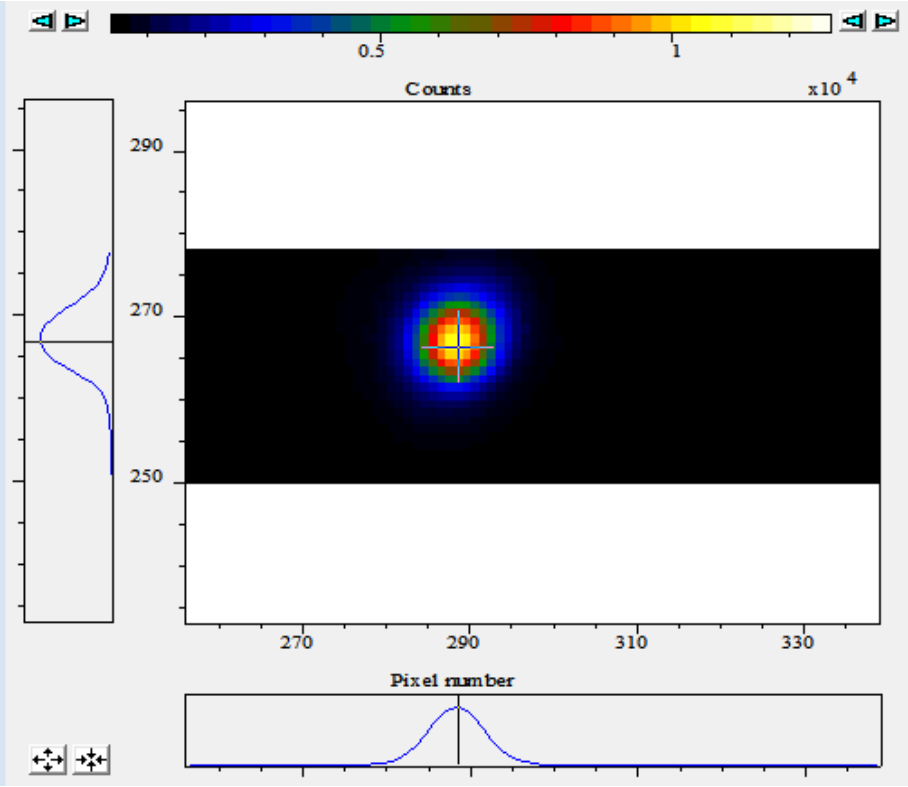

Figure 2.3: Characterization of the laser spot in the focus spot by fluorescence of a fluorescent gel.

2.3.2 Accurate Focusing and Sample Positioning.

The sample position is controlled with sub-nanometer precision in the X-Y plane by a piezo stage (MCL). The microscope objective which is used both for illumination and collection is placed on a motor with an accuracy of 25 nm in the Z direction, and together with a feedback mechanism allows maintaining good focus for a long time (days).

2.3.3 Efficient Collection for Low Emitting Samples.

The light is collected by the same objective as the illumination with a good efficiency due to the high NA. The objective used is achromatic, hence the illumination and

collection, at different wavelength would be from the same focal plane. The collected light is passed again through the dichroic beam-splitter and an emission filter. These two elements filters out the scattered laser light from the fluorescence. The fluorescence is dispersed by an imaging spectrometer which preserves a focused image on one axis and gives the emission spectrum on the second axis which gives us the ability to measure the spectrum of a single object, accurately. The light is then collected on a cooled EM-CCD (Andor) with a gain of up to 1000 with a very low background noise.

Chapter 3

Self-Assembly and Top Down Fabrication of Nanostructures

A major challenge of this field is to have a good control of the NP sizes and shapes and the precise assembly of QD-NP structures. As we have seen in the theoretical background section, this control is crucial for tuning the LSP resonance frequency as well as the coupling strength of the excited QD to the different plasmon modes.The resonance frequency depends on the type of metal and on the nanostructure size and shape, while the interaction of the QD with the different plasmon modes strongly depends on the QD-NP separation.

To address this challenge we have taken two routes: The first, developing chemical synthesis methods for producing metal NPs of different sizes, and then connecting them to QDs and forming nanostructures in aqueous solution. The second route combines top-down electron beam lithography methods for fabricating metallic NPs and our own developed process for encapsulating them with QDs embedded in silica.

3.1 Self Assembled QD-NP Structures

3.1.1 Synthesis of Metal Nanoparticle and Nanostructures

We have used a combination of methods based on previous work as well as new methods for synthesis of gold, silver or gold/silver core/shell NPs, that yield particles with diameters ranging from 5 to 200 nm with a relatively small standard deviation of their sizes (less than 10% verified by TEM). For gold and silver metal NPs of diameters 5-30 nm we use established synthesis methods based on the reduction of metal ions causing homogeneous nucleation of metal clusters in solution. For producing larger particles we have used a seeded growth approach. We start with small 20 nm metal NP solution as seeds that will grow upon reduction of additional gold or silver ions and will reach a final size depending on the initial seed concentration and metal ion concentration. In this process the final size distribution is narrower than that of the seed solution ($\sim 5\%$ standard deviation) . The reason for this size focusing is the fact that larger particles have to accumulate a larger mass of metal atoms for every increment in diameter with respect to smaller particles. The reaction results could be seen in Figure 3.1.

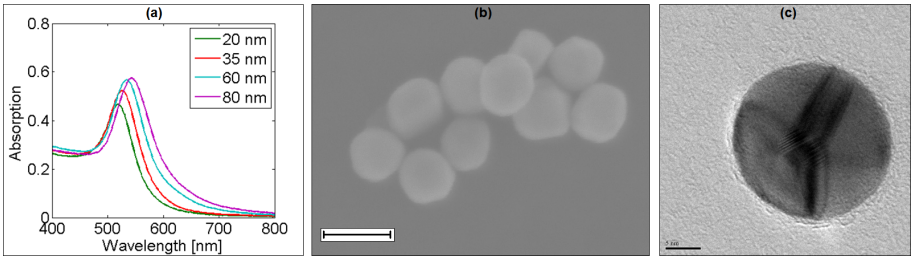

Figure 3.1: Products of the seeded growth reaction: (a) Extinction spectra of metal NPs of different sizes of gold nanoparticles 20, 35, 60 and 80 nm. (b) SEM images of 80 nm gold NPs (scale bar 100 nm). (c) TEM image of 25 nm silver NP (scale bar 5 nm).

In the aqueous base synthesis, the distance between the nanoparticles is defined by a linker molecule. With the well established commercial DNA synthesis routes, one

can get a double stranded DNA oligo-nucleotide with a predetermined sequence and a desired length ranging from 1- 800 base pairs (∼3 to 250 nm). The DNA is synthesized with a terminating reactive groups (like primary amine or thiol molecules) that could covalently bind gold or silver. The link between two metal NPs is achieved by having thiols at both ends of the DNA double strand. The link to QDs is achieved by having a DNA modified with a biotin molecule that would bind a streptavidin coated QD by a strong streptavidin-biotin bond as illustrated in Figure 3.2.

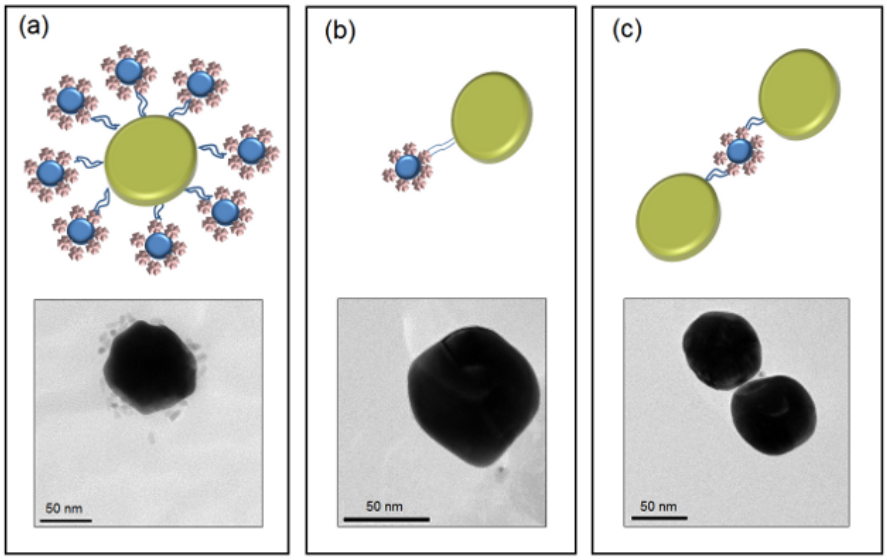

Figure 3.2: The QD-NP complexes studied in this work. The QDs (blue spheres) are surrounded by streptavidin molecules and are connected by an intermediate biotin-dsDNA-thiol molecule to 80 nm gold NPs (yellow spheres). (a) Multiple QDs attached to a single gold NP, (b) a single QD attached to a single gold NP and (c) a single QD having two DNA strands in between two gold NP (all scale bars are of 50 nm.) 10

For the case of metal NP-QD conjugates, by changing the ratio of QDs to metal NPs one can get various nanostructures. Reactions with large number of QDs per metal NPs will yields structures with a single metal NP attached to dozens of QDs as seen in Figure 3.2a. A reaction with 1:1 QD:NP ratio yields structures with a single QD attached to a single NP (Fig. 3.2b). For obtaining a structure of NP dimers with

a single QD in between we use QDs that are connected to more than a single DNA strands having two thiolated ends that bind two metal NPs.

Even though the ratio of metal NP to QD is fixed, it is inevitable to get various conjugates in each synthesis. For getting single object accuracy further purification is needed. Metal NP dimers and metal NPs with different number of QDs could be separated by gel electrophoresis. Gel electrophoresis is the gel migration of charged species under an applied voltage in an ionic solution. Figure 3.3 shows an example of gel electrophoresis separation of metal NP-QD conjugates. Metal NPs with more QDs would move slower in the gel due to their larger size. This separation is discrete because of the discrete number of QDs conjugate bound to the metal NPs. The desired fraction is then cut out and extracted from the gel .

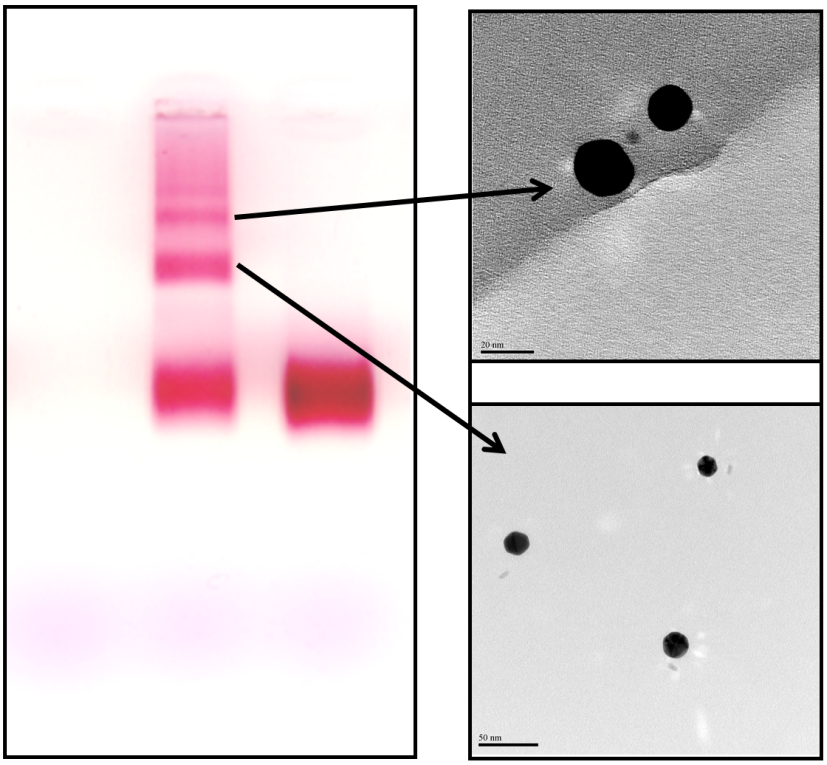

Figure 3.3: Gel electrophoresis separation of the products of a reaction of 20 nm gold metal NPs with CdSe/ZnS QDs. Conjugates migrate slower in the gel due to their larger size. The desired products are cut out of the gel and are redispersed in water.

3.2 Top Down QD - NP Structures

In the aqueous based synthesis we have made structures with multiple QDs connected to a single gold NP. The number of QDs on each NP was limited and was a few dozens at the maximum. This number of QDs is insufficient for strong Exciton-Plasmon interactions[11]. In this section we will describe the methods we have chosen for achieving this dense packing of QDs, and the measurements of exciton-plasmon interactions in these structures. We have fabricated QD-NP structures with a top down approach.

Using electron beam lithography we have fabricated arrays of metal NPs covered with a spacer layer and a densely packed layer of QDs. This fabrication methods has high yield we obtained hundreds of QD-NP structures on a single device. In the top down devices the QD-NP structures are located in a predefined position on the sample and are easily located and measured in an optical microscopy setup.

We have calculated the spectrum of local field enhancement for gold and silver hemispheres and have shown the ability to tune the LSP resonance by choosing either gold or silver and by controlling the hemisphere aspect ratio.A few examples could be shown in Figure 3.4.

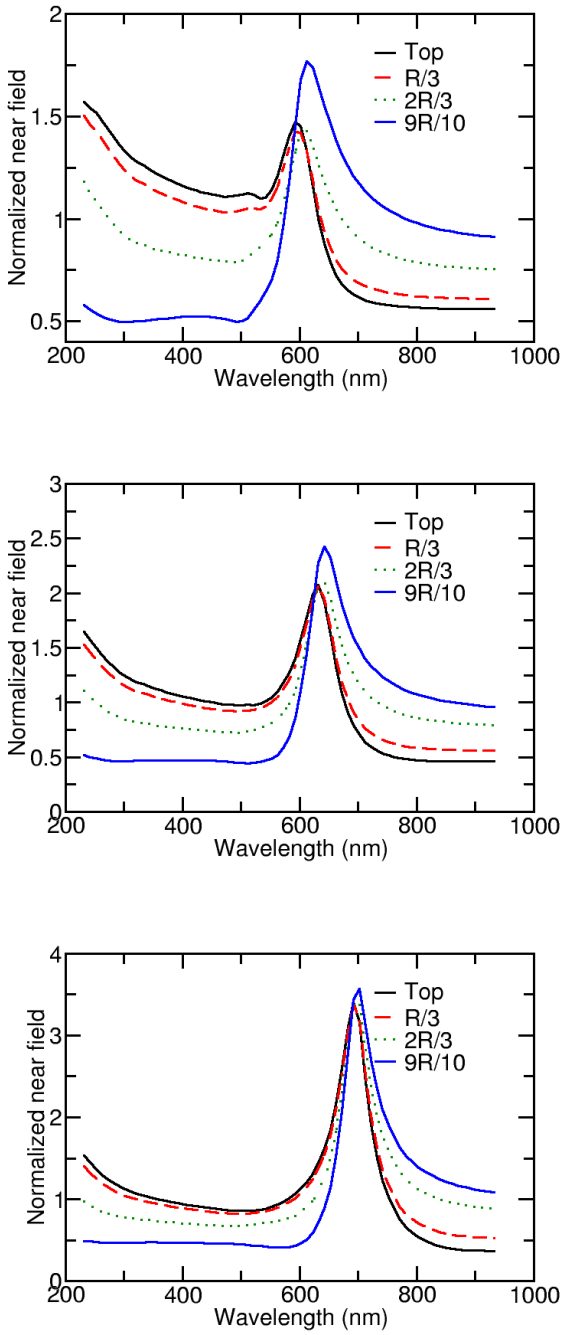

Figure 3.4: Calculations of the near field enhancement 10 nm away from a 40 nm radius hemispheres (long axis) and 40nm (top), 25 nm (middle) and 15 nm (bottom) heights. There is red shift and narrowing of the plasmon resonance as the aspect ration gets larger.

An AFM image of the structures could be seen in Figure 3.5.

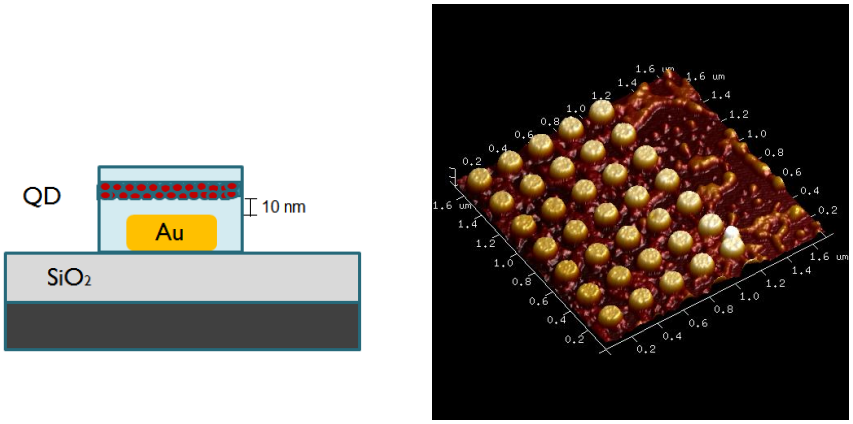

(a) (b)

Figure 3.5: The QD-NP made by top down e-beam lithography. (a) An illustration of the structures made of gold NP on $Si@Sio_2$covered with a cap of silica embedded with QDs. (b) an AFM image of the structure.

The resulting structures have a 90 nm wide scattering peak around 670 nm. This peak have a good overlap with the 640 nm emitting CdSe/ZnS QDs we use.

3.2.1 Scattering Spectra

We first characterized the plasmon resonance of the nanostructures. Extinction spectroscopy as described in the previous part could be applied only for transparent samples as in the case of gold NP in aqueous solutions. For opaque samples, as in our case, we have measured the scattering spectrum instead. In the epi-fluorescence setup as shown in Figure 3.6, white light, with a known spectrum, illuminates the sample at an obtuse angle from the bottom and the scattered light was collected by the microscope objective leaving out the specular reflected light. The collected light is dispersed by a monochromator and collected by a CCD. The results are shown in Figure 3.7.

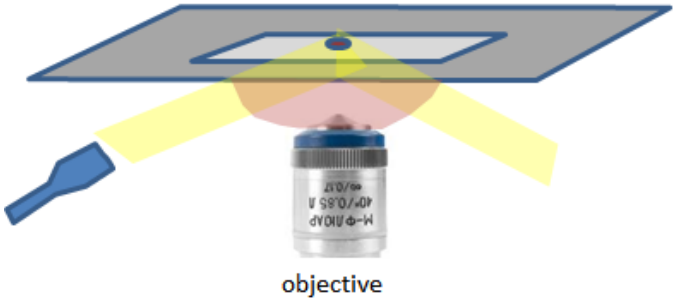

Figure 3.6: Scattering spectra setup. The sample is illuminates by white light at an obtuse angle. The scattered light is collected by an objective below the sample without collecting the specular reflected light.

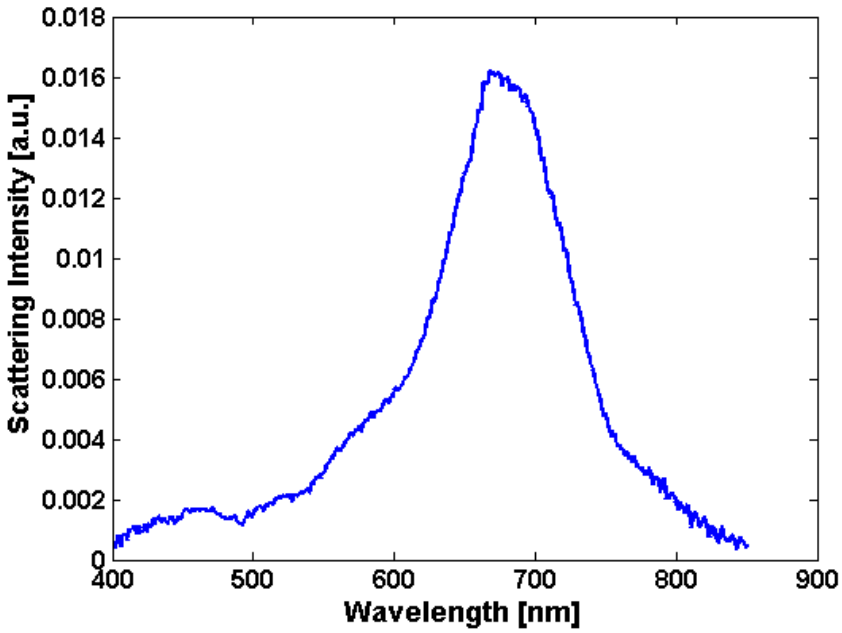

Figure 3.7: Scattering spectrum of a single silica coated gold hemisphere grown on a Si substrate.

The measured scattering spectrum of the top down assembly has a peak at 670 nm. The peak position of the spectrum is redshifted with respect to the calculated

near field of the structure (Figure 3.4b) but still has a well defined plasmon resonance that is in good overlap with the CdSe/ZnS QDs emitting at 640 nm. The reason for this change could be due to small changes between the measured structure and the calculated structure, either the thickness of the capping layer or the sharpness of the structure edges.

3.2.2 PLE Measurement of Top Down Fabricated Nanostructures.

Because of the relatively low power density of illumination, PLE measurements of a single nanostructure could not be performed in a regular spectrofluorimeter as used for solution measurements. Since we do not have a frequency tunable laser source we have conducted a measurement that compared the emission intensity of the nanostructures for only two excitation wavelengths in an epi-fluorescence configuration. For this purpose we have used two different lasers, of 532 nm and 633 nm.

We have also used this setup for measuring the power dependence of the exciton-plasmon interaction. The power tunability is achieved by inserting a linear polarizer in the beam path, just after the polarization rotator. We have calibrated the sinusoidal change in power as a function of the polarization angle in order to have a linear change in power. In addition, because of the high intensity illumination the sample heats up. To reduce this heating as much as possible we have used a high frequency chopper to chop the excitation. This way the illumination of the sample is still at the same power but has time to cool down between excitations.

Chapter 4

Plasmon-Exciton Interactions

The structures we have fabricated are well characterized and allow a quantitative study of plasmon-exciton interactions. As discussed in the introduction, the modification of the optical properties of QD in interaction can be separated into two major parts: An enhanced absorption rate of the QD and a reduction of the exciton lifetime due to coupling to different plasmon modes either radiative or non-radiative.

The QD absorption modification depends on the spatial and spectral overlap with plasmon resonance. The spectral dependence will be shown by a PLE measurement of QD-NP structures in solution while the spatial dependence will be shown in a polarization dependent measurement of single QD-NP structures.

The QD emission modification will be shown in a study of the change in the exciton decay rate.

4.1 QD Absorption Enhancement

A key aspect of our studies is the use of photoluminescence excitation (PLE) measurements as the method to obtain the QD absorption: We scan the exciting wavelength continuously over a broad range and measure the emission spectrum (Figure 4.1).

Figure 4.1b shows a comparison between the PLE spectrum of a solution of NPs connected to multiple QDs (Figure 4.1a), and a solution of bare QDs. To be able

to compare the two we normalize the spectra such that the emission intensity of the two solutions under excitation at 350 nm coincides. It is seen that the two spectra lie precisely on each other over a broad spectral range (350 nm - 480 nm), and separates as the excitation energy approaches the plasmon resonance wavelength at 560 nm. The absorption enhancement at the plasmon resonance is clearly visible.

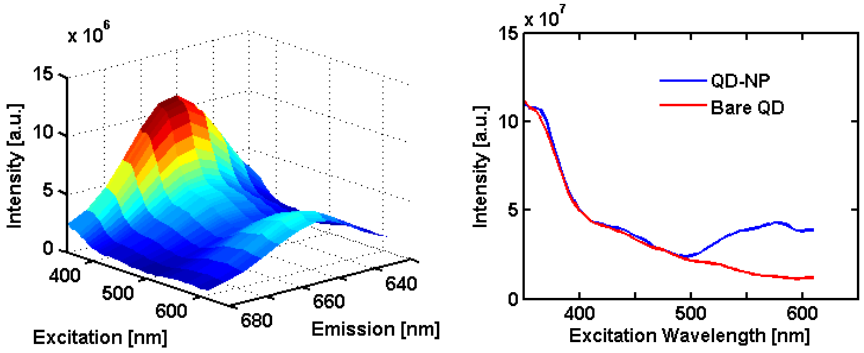

(a) (b)

Figure 4.1: Photoluminescence excitation (PLE): (a) The emission intensity as a function of excitation and emission wavelengths. The measurements are performed on aqueous solutions containing complexes of multiple QDs attached to a single gold NPs. (b) A comparison between the PLE spectra of QD-NP structures and bare QDs. The plasmon enhancement of the QD absorption around 560 nm is clearly visible.

To determine the enhancement factor we simply divide the QD-NP spectrum by that of the bare QD, and the results are shown in Figure 4.2. We perform this measurement on different QDs, with emission wavelength ranging between 565 nm - 655 nm, and observed very similar enhancement factors, ranging between 3 to 4. To compare our results with theory we calculate the local field enhancement factor as a function of the excitation wavelength for this geometry, averaging over the different incident light polarization. We use the boundary element method[30] to perform fully retarded electromagnetic calculations of NP-QD and NP-QD-NP structures. The results for cal-

culations of the the near field enhancement factor for a 80 nm gold NP could be seen in Figure 4.3.

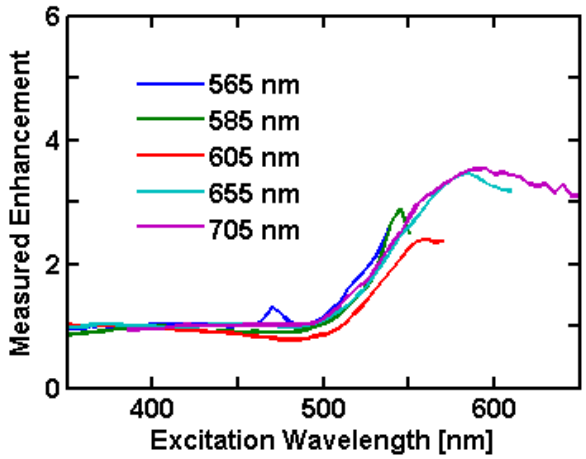

Figure 4.2: The enhancement spectrum of various QD-NP structures emitting at 565 nm, 585 nm, 605 nm, 655 nm and 705 nm.

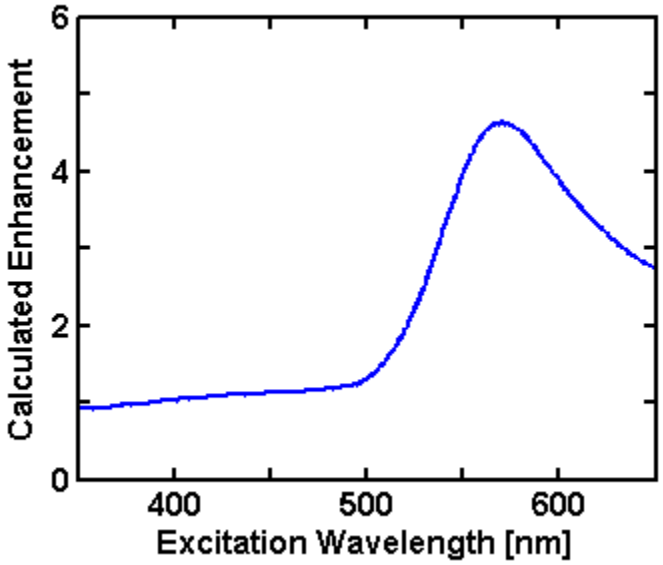

Figure 4.3: A calculation of the near field enhancement as a function of excitation, for a QD-NP structure (5 nm QD, 80 nm NP,10 nm spacing).

It is seen that the calculated wavelength dependence of the enhancement is in a very good agreement with our measurement. In particular, the measured four-fold enhancement agrees nicely with a 10 nm gap (Figure 4.3). This length is the expected gap in our structure, which consists of 20 base-pairs of double-stranded DNA (6 nm) and a streptavidin tetramer (4nm), and is verified in TEM imaging. We note that previous measurements have given enhancement factors that span a large range [22, 23, 24, 25, 31, 27, 20]. Our result resolves this ambiguity and gives a quantitative value for the enhancement factor.

We have conducted measurement of the QD absorption enhancement on the top down assembled nanostructures as well. We have compared the emission intensity of bare QDs and that of QDs coupled to the fabricated gold hemispheres. We performed the measurements at two different excitation wavelength, 532 nm and 633 nm, and by comparing the ratio of the emission intensity at theses to wavelength we could see if there is a relative enhancement or quenching of the plasmon coupled emission. The enhancement of the QD coupled to gold hemispheres was enhanced by up to a factor of 3 compared to bare QDs. The results could be seen in Figure 4.4. This result agrees well with our near field calculation having a larger intensity at 633 nm with respect to 532 nm (Fig 3.4)

On these structures, having a dense layer of QDs on each NP, we have tried to study the power dependence of the exciton-plasmon interaction. We have measured the emission intensity as a function of the incident power. When we increased the excitation power there was a difference between the behavior of bare QDs and that of the coupled QDs. Both showed saturation of the emission but at different power levels. There was also a large difference in the rate of the broadening of the spectra as a function of power.

Unfortunately under deep examination we have seen that these effects occurred along with the degradation of the sample. Hence from these measurements, although showing a qualitative change in behavior between plasmonic coupled QDs to bare QDs we cannot have a more quantitative conclusion about the interaction.

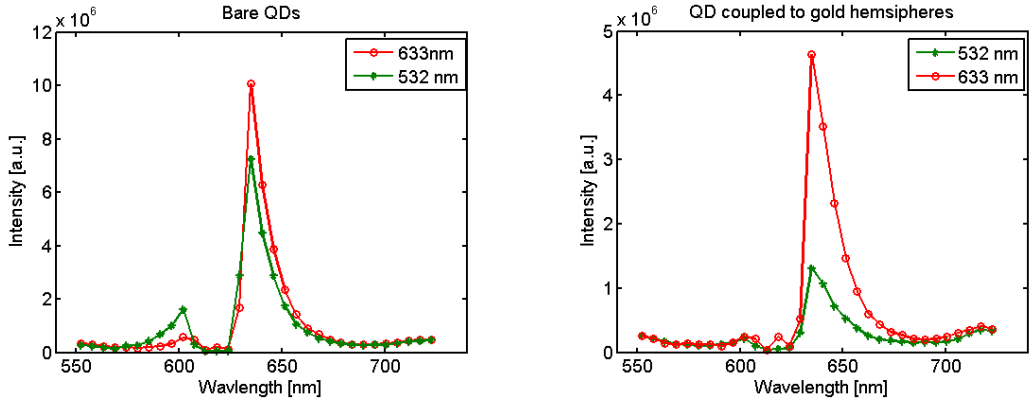

Figure 4.4: Two wavelength PLE measurement of the densely packed QD gold Hemisphere structures. The comparison of the measurements of bare QDs and that of QD coupled to gold hemispheres suggest that there is a relative enhancement of the emission between 532 nm excitation were the plasmon is off resonance comparing to 633 nm excitation which is close the plasmon resonance. This enhancement sums to about a factor of 3.

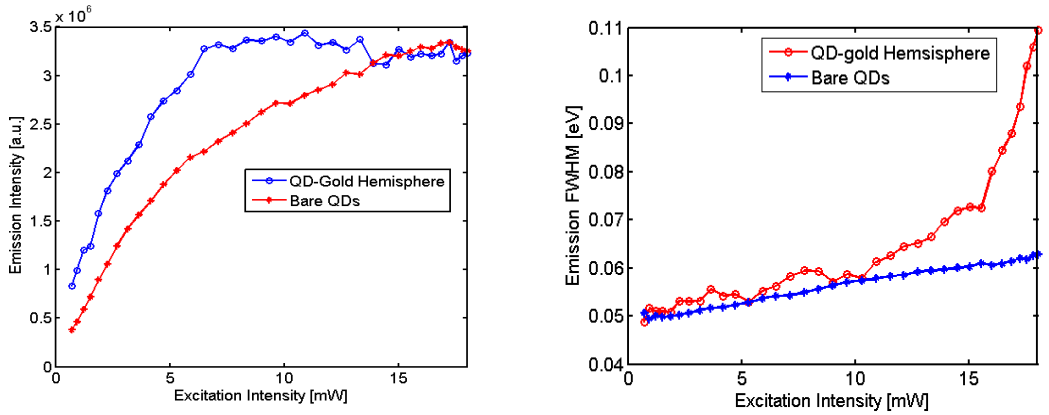

(a) (b)

Figure 4.5: Power dependent measurements. (a) The emission intensity as a function of excitation power. (b) The FWHM of the emission as a function of excitation power.

4.1.1 Single Object Measurements.

The solution measurements described above are insensitive to the incident polarization and thus average out the spatial profile of the local field enhancement. By measurements of objects consisting of a single gold NP attached to a single CdSe/ZnS QD we are able to study the underlying spatial dependence of the local field enhancement.

In order to measure the interaction on a single object level we first have to verify that we indeed measure a single QD or a single metal NP-QD conjugate. We focus a 532 nm laser to a Gaussian shaped spot with a width of 2 μm and illuminate the nanostructure at the center of the Gaussian spot. Figure 4.6 shows measurements of a single bare QD and a single metal NP-QD structure both showing emission intermittency which is an indication for emission of a single QD. In order to further verify we are dealing with a single nanostructure we correlated optical and electron microscopy images. This is demonstrated in Figure 4.7. The larger image is an overlay of two images: The first image is the scattering from the sample that shows a square grid of the sample (in gray scale). It is overlaid with an image of the emission of the NP-QD structure (red spot). The inset pictures show two SEM images of the object at two different magnifications. The lower magnification shows the same grid patterns as the optical image while the higher magnification image shows the presence of a single 80 nm in diameter gold metal NP. Due to the SEM resolution the QD is not resolved.

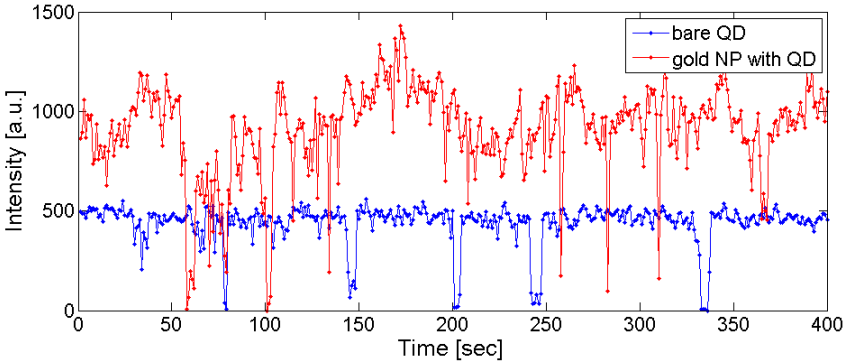

Figure 4.6: Single Bare QD and single metal NP-QD nanostructure emission intensities both showing Emission Intermittency.

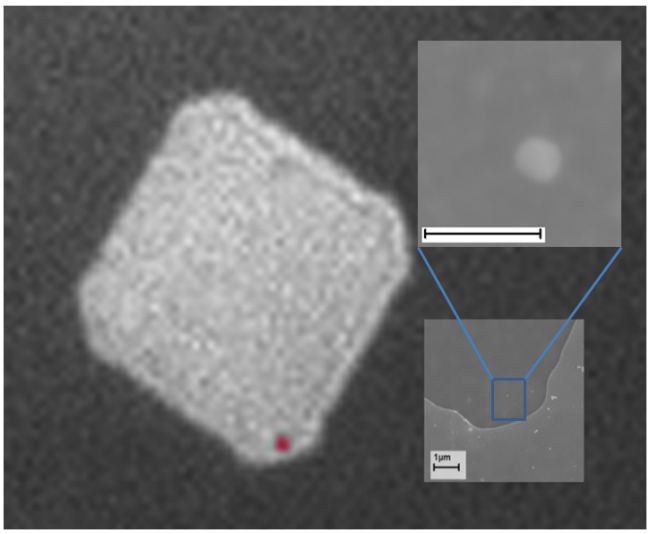

Figure 4.7: An optical image of the emission of a single metal NP-QD structure and SEM images of the same object (insets). The scale bars of the inset are 1 μm for the lower magnification and 200 nm for the higher magnification.

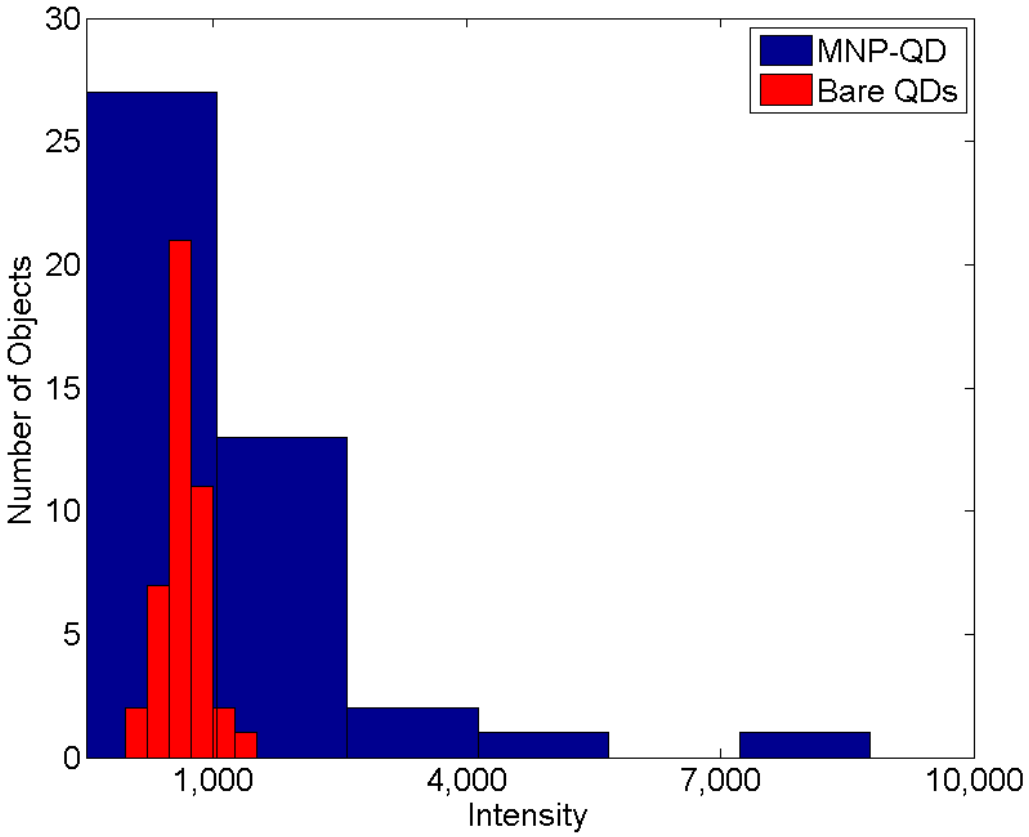

Figure 4.8: Distributions of emission intensities of metal NP-QD conjugates compared to that of bare QDs.

Figure 4.8. shows a comparison of 50 measurements of bare QDs and compare their emission intensity to that of a similar number of QD-NP structures. We find that the QD-NP ensemble exhibits a significantly broader distribution of intensities. The uniformity of our reaction products, NP and QD size as well as the QD to NP separation, suggests that the large variability in emission intensities does not originate from inhomogeneity of the objects, but is rather fundamental. We show below that the reason for this variability is the random orientation of the axis connecting the QD and the NP, relative to the laser polarization.

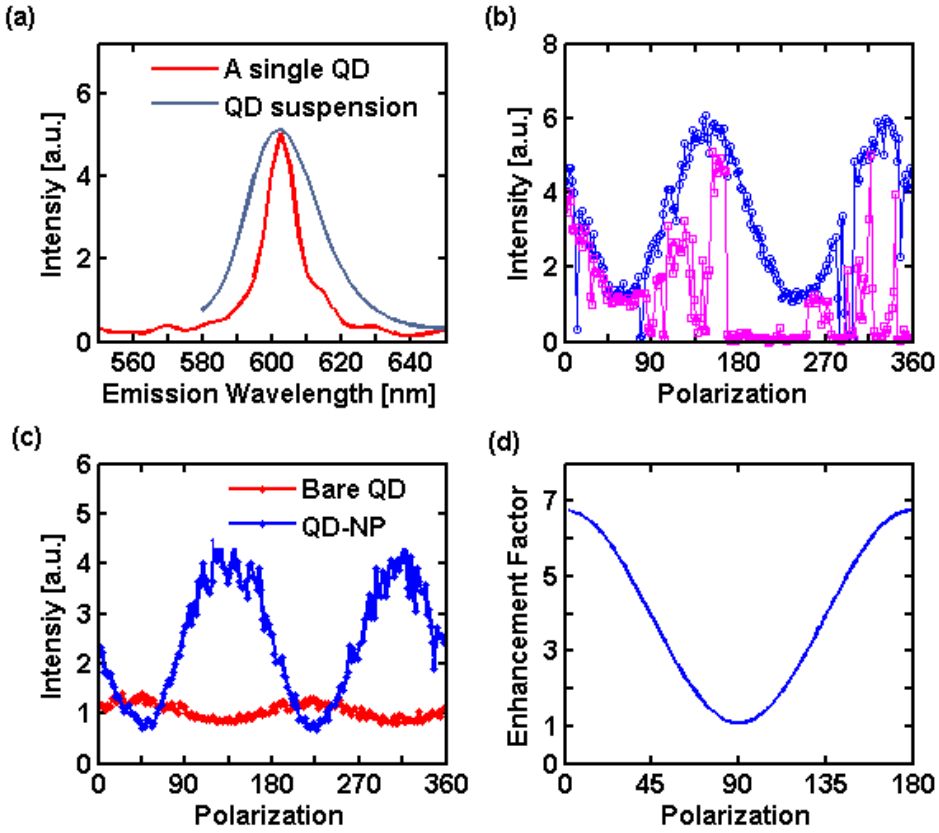

Figure 4.9: (a) A comparison of the measured emission spectrum of a single QD and of a solution of QDs. (b) Two consecutive measurements (blue and pink) of the emission intensity of a single QD while continuously varying the excitation polarization. (c) The emission intensity as a function of laser polarization for a single QD-NP and a bare QD. The data is taken by performing 5 consecutive measurements as in (b) and taking the "high" values. (d) The calculated near field enhancement factor for a QD-NP structure (5 nm QD, 80 nm NP,10 nm spacing) as a function of the excitation polarization angle with respect to the axis connecting the QD and the NP.

Figure 4.9a shows a typical emission spectrum of a single QD measured in this system (red line). It is clearly seen that the spectrum of this single object is significantly narrower than that obtained in a solution measurement (gray line), reflecting the size distribution of the QDs in a solution.

Figure 4.9b shows the emission intensity of a single QD-NP object as the excitation polarization angle is varied. It is seen that the intensity exhibits a clear and reproducible sinusoidal dependence on the polarization angle. We took special care to verify that this dependence does not originate from a measurement artifact, such as slight movement of the excitation spot with the rotation of the polarization. Indeed, the maximum for different objects appears at different angles. This proves that the observed dependence is due to the relative orientation of the QD-NP axis relative to the laser polarization. It is seen that the sample shows emission intermittency, which is a characteristic of a single QD measurement, and in the following discussion we consider the highly emitting state only.

Figure 4.9c compares the polarization dependence of a bare QD and a single QD-NP structure. We present the curve of a QD-NP object, which exhibits the largest contrast, presumably because its axis is parallel to the cover-slip plane. Objects that are oriented at an angle to this plane would have lower polarization dependence. We note that there is a weak polarization dependence also in the bare QDs measurement. This is probably related to an asymmetry in the QD shape [32, 33]. The sinusoidal dependence of the QD-NP objects agrees well with the expected plasmonic behavior: the near field around the metal sphere is maximal along the laser polarization axis, and minimal perpendicular to it. As we rotate the laser polarization we move the maximum and minimum around the NP, and consequently modify the local field experienced by the QD. At the peak of the curve we find that the emission intensity of the QD-NP is enhanced relative to the bare QD, by approximately a factor of four, while the intensity at the minimum is suppressed. Figure 4.9d shows the calculated polarization dependence of the enhancement factor for a 10 nm gap. It is seen that the contrast ratio between minimum and maximum values, which is approximately 7, agrees very well with that found experimentally. This calculation describes only the enhancement of the local field at the QD. The measured emission intensity is a product of this enhancement curve and the modified quantum efficiency, which is ~ 0.5 at this wavelength (Fig. 4.12). The modification of the quantum efficiency is due to energy transfer from the QD to the

metal NP due to excitation of non-radiative high order plasmon modes, as discussed in the theoretical background.

The strong polarization sensitivity is further enhanced in NP-QD-NP structure (Figure 3.2c). Figure 4.10a shows the polarization dependence of the emission intensity for a single NP-QD-NP object, and compares it to a bare QD (its average is taken to be 1). Again, a sinusoidal dependence is observed, but this time with a contrast ratio, which is close to 100. Figure 4.10b shows a calculation of the near field intensity for this structure. We find that the contrast ratio is maximal when the QD is located on the axis between the spheres, and drops as the QD shifts away from this axis. This maximum is close to 100 for the parameters of our sample, in a very good agreement with our findings. This observation demonstrates the strength of plasmonic structure design in tailoring the optical properties of a QD.

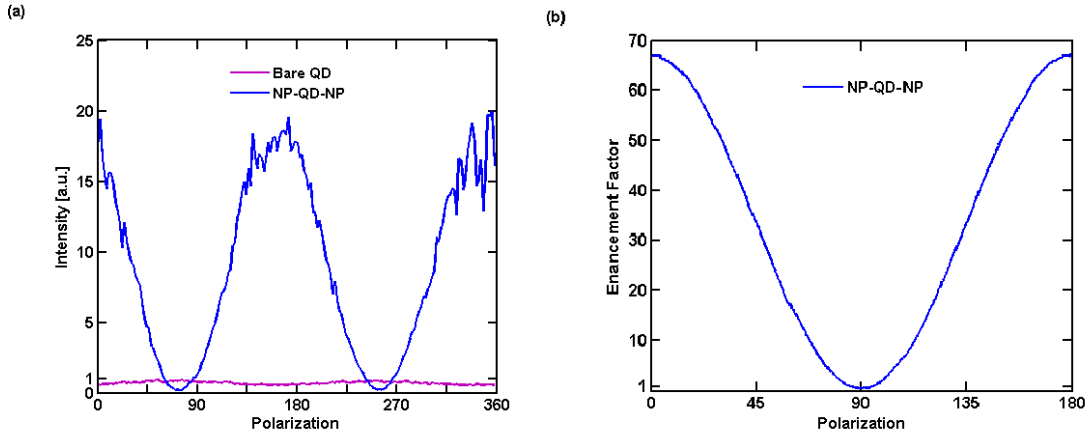

Figure 4.10: NP-QD-NP structure measurements. (a) Emission intensity of a single NP-QD-NP structure as a function of the polarization angle. We obtain up to 20 fold enhancement with respect to a typical bare QD, and there is 85:1 contrast between the maximal intensity to the minimal intensity. (b) Calculated near field enhancement for a NP-QD-NP structure (5 nm QD, 80 nm NP,5 nm spacings).

4.2 Modification of the Exciton Decay Rate

To obtain a complete picture of the QD-NP interaction we conduct time resolved measurements of the QD exciton emission.

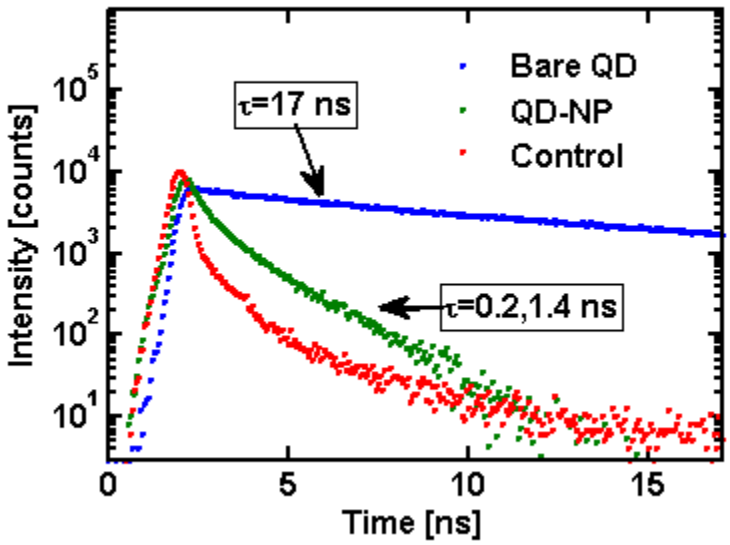

Figure 4.11: Time resolved fluorescence decay measurements of bare QDs (blue) and QD-NP structures (green) (The system response is shown in red). The large decrease of the exciton lifetime in the QD-NP structures is clearly visible.

Figure 4.11 compares the emission lifetime of bare QDs and QD-NP structures in solution. The bare QDs lifetime could be easily resolved within our time resolution, and is found to be 17 ns. It is seen that the QD-NP lifetime is much shorter, and is comparable to our time resolution. Using an iterative fitting process, in which the measured system response is convolved with exponential decay rates, the QD-NP data could best be fit to two exponential decay rates, of 0.3 ns and 1.4 ns.

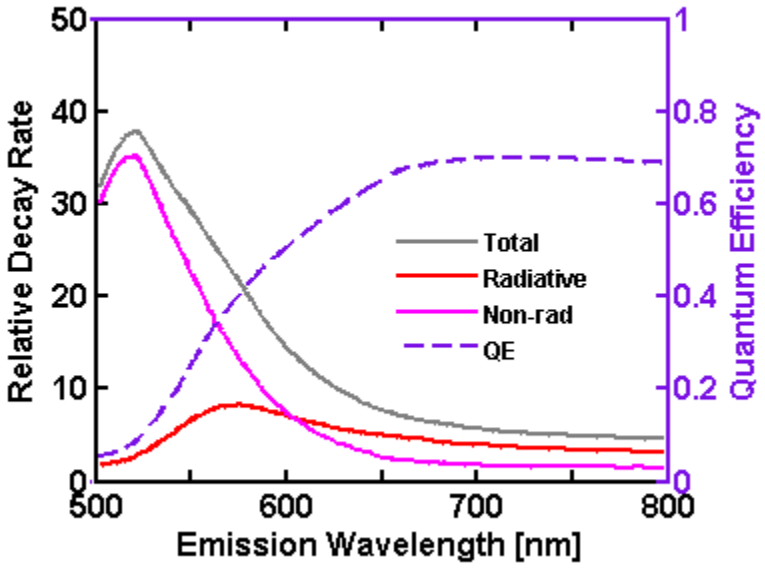

Figure 4.12: Calculation of the radiative and non-radiative decay rate of QD-NP (relative to a bare QD) and the quantum efficiency as function of the emission wavelength.

Figure 4.12 shows the calculated enhancement of the decay rates for a 10 nm gap QD-NP structure. It is seen that the total decay rate, which is the sum of the radiative and non-radiative rates, increases by more than an order of magnitude at 605 nm, in good agreement with the observed result. We note that both rates should be enhanced in the QD-NP structure relative to the bare QD, and the quantum efficiency, which is the fraction of the radiative rate from the total, becomes approximately 0.5 at 600 nm, and may go down to 0.05 at 520 nm due to strong absorption in the gold NP.

Chapter 5

The Plasmon Resonance Spectrum

As seen in the introduction plasmon oscillations have eigen modes with well defined resonance frequencies. One can naively conclude that in different measurements of the plasmon resonance, either far field measurements, like scattering or extinction, or near field measurements, the peak frequency will be of the same value. Surprisingly, full electromagnetic calculations show that the there is a difference between the far field and the near field spectra: the near field spectrum is red shifted and broadened relative to the far field. While the difference is well known theoretically there is no direct experimental measurement of it. The reason for this lack of experimental evidence is the difficulty in measuring the near field spectrum.

In this chapter we address this problem. We first provide an intuitive model for the optical response of gold NPs in terms of a simple harmonic oscillator. We show that this simple model qualitatively explains the shift, and provides a physical mechanism for it. We then measure the near and the far field spectra of gold NPs and demonstrate the expected changes. We find that there is a significant difference between the measured peak frequency and width of the near field intensity spectrum and the measured scattering and extinction spectrum. We discuss our result in the context of an harmonic oscillator model as well as full electrodynamic calculations of the optical response of gold NPs.

5.1 Harmonic Oscillator Model for Plasmon Resonance

In this section we follow a derivation given in reference [34]. The motion of electrons in metal NPs can be modeled by a harmonic oscillator. The equation of motion for the electron displacement, $x(t)$, is:

$$m_e\ddot{x(t)} + m_e\gamma\dot{x(t)} - kx(t) = F(\omega, t) \tag{5.1}$$

The motion is driven by a force, $F = F_0 cos(\omega t)$ exerted on the electrons by an external electromagnetic field at optical frequencies. The polarization created by the electron motion creates a restoring force on the electrons, which we model as a spring with a constant k and a force proportional to the electrons displacement, $-kx$. The damping of the electron motion is represented by a friction force proportional to the velocity with a damping rate, γ.

The solution to equation 5.1 is:

$$x(t) = \frac{F_0/m_e}{\sqrt{(\omega_0^2 - \omega^2)^2 + (\gamma\omega)^2}} \cdot cos(\omega t + \delta) \tag{5.2}$$

where $\omega_0 = \sqrt{\frac{k}{m}}$, and $tan(\delta) = \frac{\gamma\omega}{\omega_0^2 - \omega^2}$.

The maximal amplitude for this motion is obtained for a frequency which is red shifted with respect to the natural frequency ω_0,

$$\tilde{\omega} = \sqrt{\omega_0^2 - \gamma^2/2} \quad . \tag{5.3}$$

The relation of the maximal amplitude of electron motion to the local electric field is quite straight forward. The displacement of electrons from their equilibrium position generates an electric field, and its maximal amplitude occurs at the frequency where the amplitude of the electron motion is the largest, i.e. at $\tilde{\omega}$, the red shifted frequency.

We can infer that the electromagnetic energy stored in the electromagnetic near field is related to the potential energy of the oscillator,

$$\langle U(t)\rangle = \left\langle \frac{1}{2}kx(t)^2 \right\rangle = \frac{1}{2}k\left\langle x(t)^2\right\rangle \tag{5.4}$$

$$= \frac{1}{2}k\frac{F_0^2}{m_e^2}\cdot\frac{1}{(\omega_0^2-\omega^2)^2+(\gamma\omega)^2}\cdot\left\langle cos^2(\omega t+\delta)\right\rangle = \frac{1}{4m}\omega_0^2F_0^2\frac{1}{(\omega_0^2-\omega^2)^2+(\gamma\omega)^2} \tag{5.5}$$

Indeed, we can see that the potential energy peaks at the same position as the maximal amplitude of the oscillator, $\tilde{\omega} = \sqrt{\omega_0^2 - \gamma^2/2}$.

5.1.1 The Power Spectrum of a Harmonic Oscillator

In a similar manner the extinction spectrum of the plasmon resonance can be related to the total energy absorbed by the oscillator. The absorption of energy is the work per unit time exerted by the external force on the oscillator:

$$P = F\cdot\dot{x}(t) \tag{5.6}$$

which gives:

$$P = F_0cos(\omega t)\cdot\frac{-2\omega}{(\omega_0^2-\omega^2)^2+(\gamma\omega)^2}\cdot\omega sin(\omega t-\delta) \tag{5.7}$$

Taking a time average over a full period of oscillation we get:

$$\langle P(t)\rangle = \frac{F_0^2\gamma}{2m_e}\cdot\frac{\omega^2}{(\omega_0^2-\omega^2)^2+(\gamma\omega)^2}. \tag{5.8}$$

Looking at this expression, we could see that the total absorbed power peaks at the natural driving frequency $\omega = \omega_0$. It is thus seen that for this model the extinction spectrum and the near field spectrum peak at different frequencies.

5.2 The Optical Properties of Metal NPs

A more realistic approach is obtained by a direct solution of the electric field in response to optical excitation. In the introduction we have presented the solution of the far field

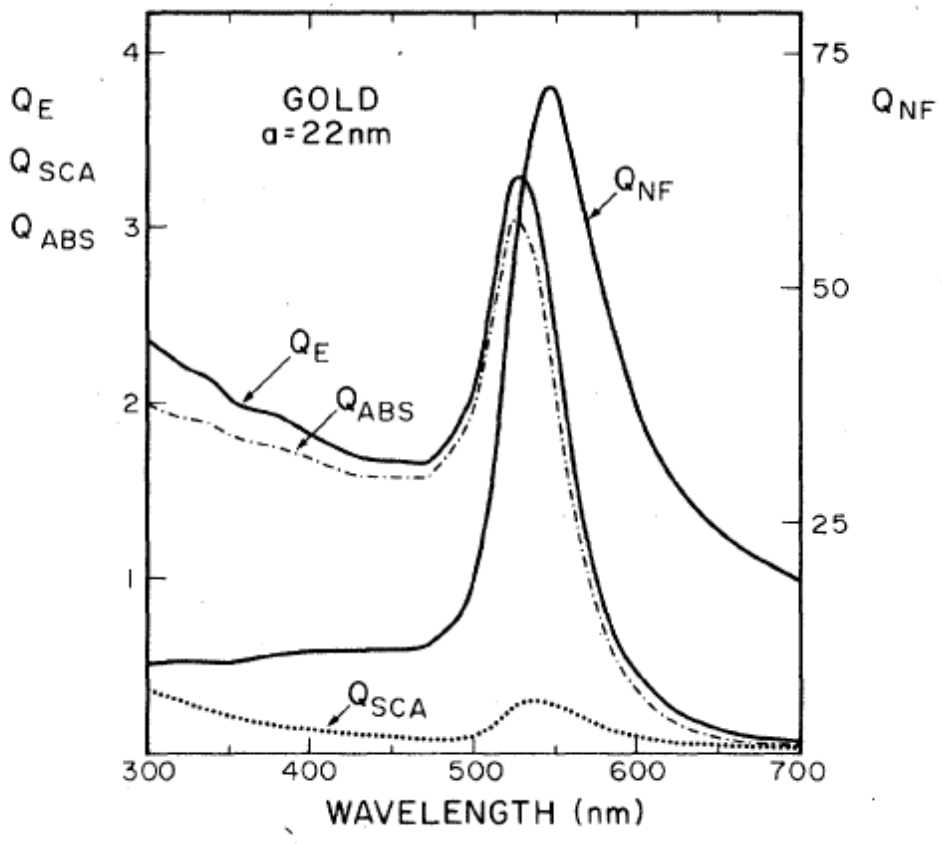

Figure 5.1: (a) Mie Theory calculation of the extinction spectra of gold NP of different diameters. (b) Near field and far field calculations for gold NPs [35].

in the context of Mie theory. A solution for the near field spectrum of gold NPs can be similarly obtained [35].

Figure 5.1 presents a calculation of the various optical spectra of a 22 nm gold NP. It presents the absorption, scattering, and extinction spectra as well as the near field spectrum. It is seen that the near field spectrum is red shifted and broadened with respect to the extinction spectrum, consistently with the results of the harmonic oscillator model. However, it is seen that unlike the oscillator model, in this calculation the spectrum is broadened as well.

The scattering spectrum is presented in the dotted curve. It is seen that the scattering efficiency is much smaller than the absorption and its contribution to the total

extinction (which is the sum of the scattering and absorption) is minor. The scattering intensity is proportional to the NP volume and for a NP of around 100 nm becomes the dominant part of the total extinction. (Figure 1.3 on page 19.)

A small redshift of the scattering spectrum with respect to the absorption spectrum is observed as well. As we have discussed in the introduction, Unlike the red shift of the near field, which originates from simple damping, the red shift of the scattering is due to a different mechanism, it is due to a retardation effect, and becomes larger for large NPs.

5.3 Plasmon Spectroscopy

In the following, we show a comparison of the extinction, scattering and the near field spectra, measured on the same sample of gold NPs. We would like first to point out the difficulty of the study and the uniqueness of the results.

The frequency dependent far field properties, the extinction and scattering cross-sections, are easily measured by illuminating a sample and collecting the light transmitted or scattered by the it. However, there is no straight forward way to measure the near field spectrum of plasmonic structures, as the sizes and resolution of current near field probes and microscopes are larger than the sizes of typical nanostructures. Moreover, inserting a large probe in the vicinity of a plasmonic structure will alter the dielectric environment and will have a strong impact on the plasmon resonance.

It should be noted that all of the work we know of in the context of probing the near field by molecular emission or SERS, probe the near field integrated intensity at a limited spectral range and does not give the full spectral information. As we have seen in the PLE measurements we have conducted, QDs can serve as probes for the near field spectrum of gold NPs. We will show that our measurements, allow us to probe directly the near field spectrum of gold NPs and to compare it with the far field spectra.

A PLE measurement on a single nanostructure is difficult to realize over a broad

spectral range. The main difficulty is the need to filter the scattered light (which require spectral filters) and to have a fully achromatic optical setup. We have been able to probe only two excitation wavelengths in our experiment described in Chapter 4. Furthermore, scattering measurements of a single plasmonic nanostructure are possible only for objects larger then ~100 nm, and may have a large variation from one object to another. These difficulties imply that measurements of a single object are not feasible and we should use ensemble measurements in solution instead.

In order to measure the near field in an ensemble, the nanostructures have to be similar in shape and in the distance of the QD from the gold NP. This is exactly the strength of our technique. We have achieved that goal by our synthetic route as describe in Chapter 2. In the following, we describe the results of ensemble measurements in solution.

5.3.1 Far-Field Spectra - Extinction and Scattering

We begin with measurements of the extinction spectrum of gold NPs. For our experiment we have used 80 nm gold NPs. The extinction spectrum of 80 nm gold NP peaks at 548 nm as could be seen in Figure 5.3.

We have fitted the extinction spectra to the harmonic oscillator model (on an energy scale). The extinction spectrum and the fit could be seen in Figure 5.2.

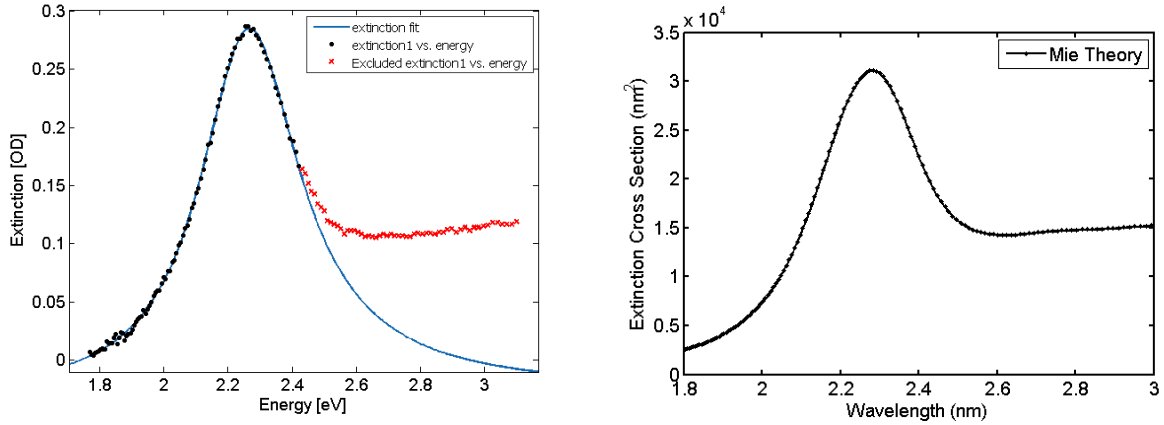

(a) (b)

Figure 5.2: (a) The extinction spectrum of gold NPs fitted to the power absorption of the harmonic oscillator model. (b) Mie theory calculation of the extinction cross-section. The spectrum is presented on an energy scale for comparison.

From the fit we extract the decay rate of the plasmon , γ and calculate the expected shift in the near field spectrum $\tilde{\omega} = \sqrt{\omega_0^2 - \gamma^2/2}$. The results give a small shift of 2 nm, and a width of 82 nm.

We have also calculated the extinction cross section for 80 nm gold NP in water, using Mie theory. The results for the peak position and width are, 543 nm and 84 nm respectively, in reasonable agreement with our measurements. The difference can be attributed to non perfect spherical shape of the measured NPs, change in size and dielectric environment.

The following measurement demonstrates the dependence of the extinction spectra on the NP size. The extinction spectra of 80 nm and 17 nm gold NPs could be seen in Figure 5.3. It is seen that the 17 nm diameter gold NP has extinction maximum at 518 nm, 30 nm away from the 80 nm NPs peak. The extinction spectra of 80 nm and 17 nm gold NPs could be seen in Figure 5.3.

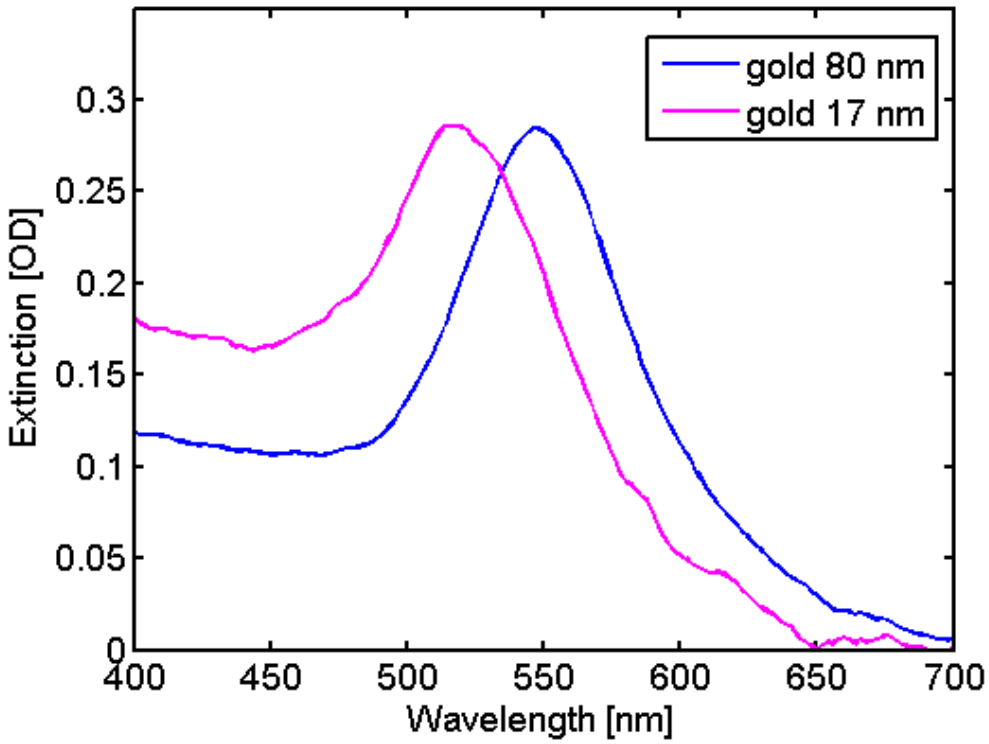

Figure 5.3: Extinction spectra of 17 nm and 80 nm gold NPs solutions. The 17 nm extinction spectrum is normalized to have the same peak height of the 80 nm spectrum, for comparison.

The shift in the extinction spectrum originates from the enhancement and the shift of the scattering component of the total extinction, and could be seen in the direct measurement of the scattering of the sample. The scattering spectrum of the same gold NPs peaks at a red shifted wavelength of 560 nm (Figure 5.4). As discussed above, the redshift of the scattering for large NPs is known to originate from retardation effect. Hence, the extinction, which is the sum of the absorption and scattering, peaks at a shorter wavelength, 12 nm away.

In order to compare the near field and the far field spectra, we first have to be convinced that indeed the presence of the QDs does not alter the plasmon resonance, otherwise the QDs would not serve as good probes for the plasmon resonance near field.

We have verified that this is the case by comparing the scattering spectra of bare gold NPs and QD-NP structures as can be seen in Figure 5.4.

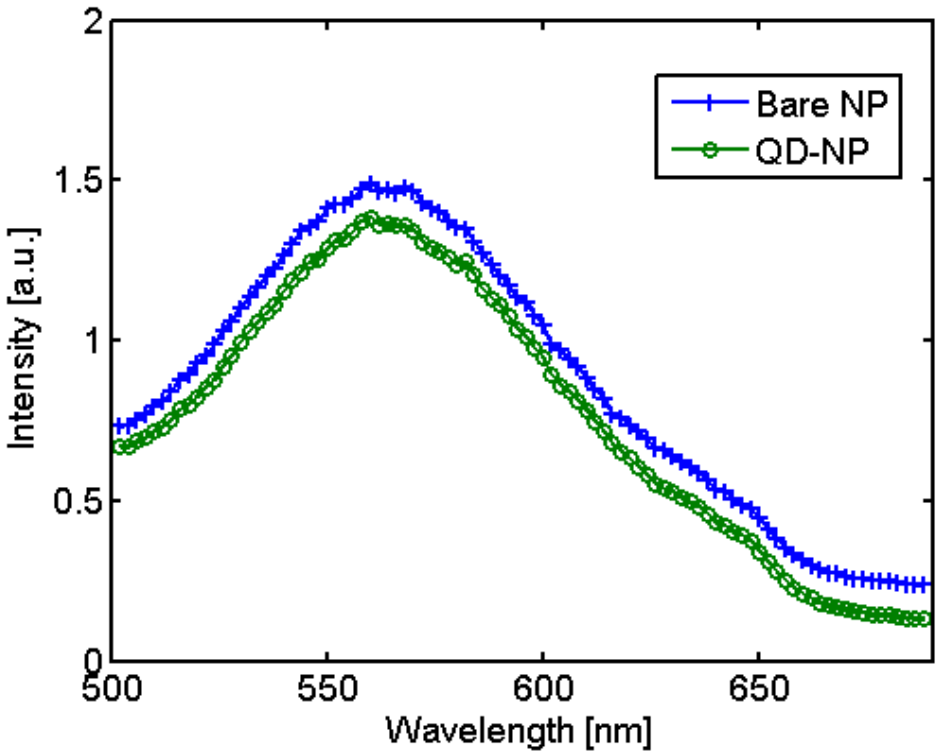

Figure 5.4: A comparison of the scattering spectra of 80 nm gold NPs and NP-QD structures. The spectra are shifted in the intensity scale for visibility.

5.3.2 The Near-Field of the Plasmon Resonance

Results of PLE measurements of NP-QD structures consisting of 80 nm gold NP and CdSe/ZnS QDs emitting at 655 nm is shown in Figure 5.5.

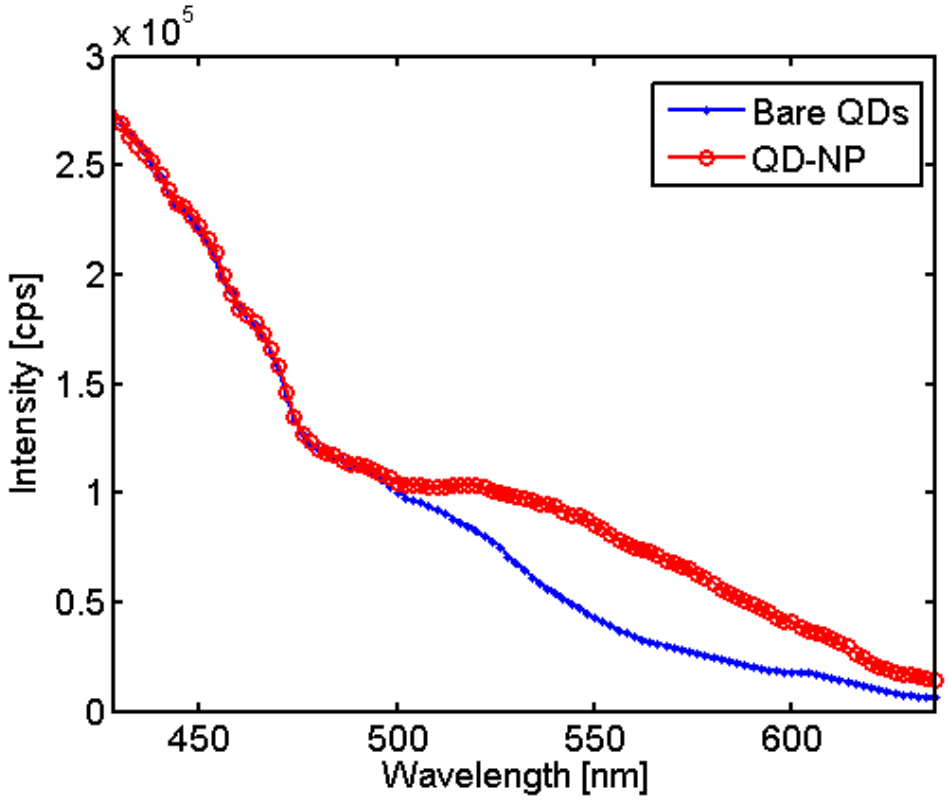

Figure 5.5: PLE measurements of Bare QDs Vs. QD-NP structures. The emission is probed at 660 nm. There is a large enhancement in the region between 500 and 600 nm corresponding to the local field enhancement of the plasmon resonance.

The near-field intensity of the plasmon resonance can be derived from the ratio of the total QD-NP emission to the emission of bare QDs at the same excitation wavelength. Probing the near field intensity at different wavelengths yields the near-field spectrum of the structure. Figure 5.6a shows the near field spectrum of 80 nm gold NP as probed by the QDs emission.

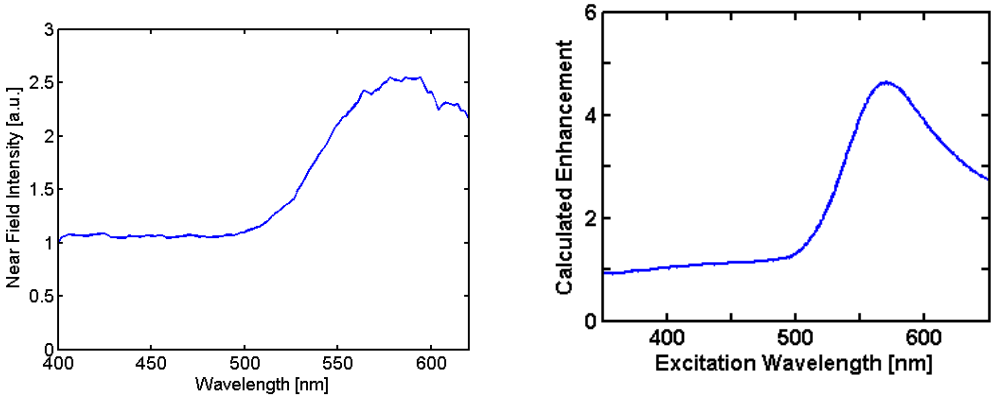

(a) (b)

Figure 5.6: (a) The near field spectrum of 80 nm gold NPs, as extracted from PLE measurements of NP-QD nanostructures.. (b) Calculation of the near-field enhancement at a distance of 7 nm from a 80 nm gold NP.

The near-field enhancement peaks at 584 nm and has a half width of 47 nm. Numerical calculations (performed by G. Bryant for our study) of the near field of 80 nm gold NP at a distance of 7 nm from the surface could be seen in Figure 5.6b. The resonance peaks at 570 nm and has a half width of 35 nm.

Our measurements show that the near field spectrum peak is red shifted by 36 nm with respect to the measured extinction peak. The harmonic oscillator model gives a red shift of only 2 nm, and clearly can not quantitatively explain the large is shift that is observed in the measurements.

On the other hand, if we compare the peak position of the Mie extinction cross section and the peak of the near field calculation we obtain a redshift of 27 nm which is closer to the measured shift.

Figure 5.7 summarizes our findings, and shows the three spectra, extinction, scattering and the near field. For convenience, we have normalized them to the same height.

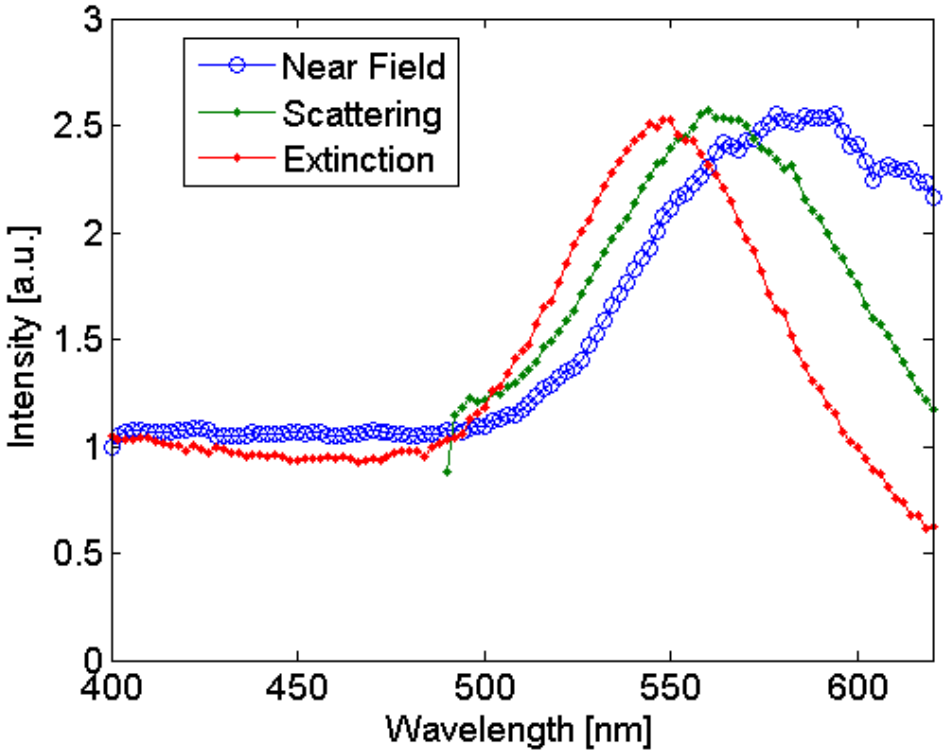

Figure 5.7: The Near Field spectrum of 80 nm gold NPs extracted from a PLE measurement of NP-QD structures (blue). The Near Field spectrum peaks at a red shifted wavelength of 584 nm. The scattering (green) and extinction (red) spectra of similar gold NPs are presented and normalized for reference.

The shift of the scattering spectrum relative to the extinction spectra, as mentioned, is explained by the electric field retardation. There is a an even larger red shift and broadening of the near field spectrum. The shift is due to the damping of the plasmon oscillations.

The exact measurement of this shift is important. We have seen that calculations does not give the exact near field spectrum. Direct measurements of the near field spectrum are thus crucial for designing plasmonic devices that manifest near field interactions.

Chapter 6

Discussion

We have developed reproducible methods for the synthesis gold NPs by wet chemistry as well as by e-beam lithography. The synthesized NPs have a well characterized plasmon resonance which is important for conducting a quantitative study of plasmon-exction interaction. The solution based structures reach a high purity level due to adoption of biosynthetic methods such as DNA and protein based self-assembly as well as gel electrophoresis purification. The use of QDs which are observable in TEM, allows us to determine the QD-NP separation as well as the exact number of QD and NPs in the structure.

The top down structures we have developed have a dense layer of QDs in a well define distance from the NP surface. These structures open a way for measuring exciton-plasmon interaction in the strong field regime.

Using these structures we have demonstrated the modification of the absorption and emission properties of the QD due to exciton-plasmon interaction. PLE measurements of the QD-NP structures show enhancement of the absorption in regions of spectral overlap between the plasmon resonance and the QD absorption band. Through these PLE measurements we directly measure the near field spectrum of the plasmon resonance. This result is unique to our knowledge. It is achievable due to the broad absorption band of QDs that allows the observation of the onset plasmon resonance. This requires

a sample of high purity, consisting only of QD-NP structures, any unbound QDs will result in a bias to the measurement.

Lifetime measurements show an increased exciton decay rate as predicted by numerical calculations and by our theoretical model as well.

A major result of this work is the measurements of plasmon-exciton interaction on a single object level. Unlike the small enhancement factors which are the usual results for ensemble average measurements, for single QD-NP structures the absorption is enhanced by an order of magnitude and by up to two orders of magnitude for NP-QD-NP structure . Moreover, by changing the polarization of the excitation we were able to tune the spatial overlap of the plasmon and exciton resonances and observe a change of the absorption enhancement ranging from zero up to the maximal enhancement factor.

In these measurements the QD serves as a probe for the near field spatial distribution of the plasmon resonance. In this way we could separate the polarization dependent plasmonic near field, causing a varying absorption rate in the nearby QD, from the modification of the exciton decay rate which does not depend on the polarization of the excitation.

This work gives a wholesome description of the exciton-plasmon interactions, consistent with theoretical models and provide solid explanation for many of the experimental ambiguities in this field.

Bibliography

[1] Faraday, M. The Bakerian Lecture: Experimental Relations of Gold (and Other Metals) to Light. 1857.

[2] Mie, G. *Annalen der Physik* **1908**, *330*, 377–445.

[3] Ritchie, R. H. *Phys. Rev.* **1957**, *106*, 874–881.

[4] Kreibig, U.; Vollmer, M. *Optical Properties of Metal Clusters*; Lecture Notes in Economic and Mathematical Systems; Springer, 1995.

[5] Raether, H. *Surface plasmons on smooth and rough surfaces and on gratings*; Springer tracts in modern physics v. 111; Springer, 1988.

[6] Barnes, W. L.; Dereux, A.; Ebbesen, T. W. *Nature* **2003**, *424*, 824–30.

[7] Maier, S. A.; Atwater, H. A. *Journal of Applied Physics* **2005**, *98*, 011101.

[8] Ozbay, E. *Science* **2006**, *311*, 189–193.

[9] Altewischer, E.; van Exter, M. P.; Woerdman, J. P. *Nature* **2002**, *418*, 304–6.

[10] Bergman, D.; Stockman, M. *Physical Review Letters* **2003**, *90*, 027402.

[11] Noginov, M. A.; Zhu, G.; Belgrave, A. M.; Bakker, R.; Shalaev, V. M.; Narimanov, E. E.; Stout, S.; Herz, E.; Suteewong, T.; Wiesner, U. *Nature* **2009**, *460*, 1110–2.

[12] Stockman, M. I. *Nature Photonics* **2008**, *2*, 327–329.

[13] Novotny, L.; Hecht, B. *Principles of Nano-Optics*; Principles of Nano-optics; Cambridge University Press, 2006.

[14] Maier, S. A. *Plasmonics: Fundamentals and Applications*; Springer, 2007.

[15] Marder, M. *Condensed matter physics*; Wiley-Interscience; John Wiley, 2000.

[16] Kittel, C. *Introduction to Solid State Physics*; Wiley, 2004.

[17] Yguerabide, J.; Yguerabide, E. E. **1998**, *156*, 137–156.

[18] Alsawafta, M.; Wahbeh, M.; Truong, V.-V. *Journal of Nanomaterials* **2012**, *2012*, Article ID 457968.

[19] Metiu, H. *Progress in Surface Science* **1984**, *17*, 153 – 320.

[20] Zhang, J.; Fu, Y.; Chowdhury, M. H.; Lakowicz, J. R. *Nano Letters* **2007**, *7*, 2101–7.

[21] Kulakovich, O.; Strekal, N.; Yaroshevich, A.; Maskevich, S.; Gaponenko, S.; Nabiev, I.; Woggon, U.; Artemyev, M. *Nano Letters* **2002**, *2*, 1449–1452.

[22] Anger, P.; Bharadwaj, P.; Novotny, L. *Physical Review Letters* **2006**, *96*, 3–6.

[23] Govorov, A. O.; Bryant, G. W.; Zhang, W.; Skeini, T.; Lee, J.; Kotov, N. A.; Slocik, J. M.; Naik, R. R. *Nano Letters* **2006**, *6*, 984–994.

[24] Lakowicz, J. R. *Plasmonics (Norwell, Mass.)* **2006**, *1*, 5–33.

[25] Lee, J.; Govorov, A. O.; Dulka, J.; Kotov, N. A. *Nano Letters* **2004**, *4*, 2323–2330.

[26] Mertens, H.; Biteen, J. S.; Atwater, H. A.; Polman, A. *Nano Letters* **2006**, *6*, 2622–5.

[27] Shimizu, K.; Woo, W.; Fisher, B.; Eisler, H.; Bawendi, M. *Physical Review Letters* **2002**, *89*, 9–12.

[28] Gueroui, Z.; Libchaber, A. *Phys. Rev. Lett.* **2004**, *93*, 166108.

[29] Nooney, R. I.; Stranik, O.; McDonagh, C.; MacCraith, B. D. *Langmuir* **2008**, *24*, 11261–11267, PMID: 18771301.

[30] Aizpurua, J.; Bryant, G. W.; Richter, L. J.; García de Abajo, F. J. *Physical Review B* **2005**, *71*, 235420–1 – 234520–13.

[31] Mertens, H.; Koenderink, A.; Polman, A. *Physical Review B* **2007**, *76*, 1–12.

[32] Suo, B.; Su, X.; Wu, J.; Chen, D.; Wang, A.; Guo, Z. *Materials Chemistry and Physics* **2010**, *119*, 237 – 242.

[33] Acharya, S.; Panda, A.; Efrima, S.; Golan, Y. *Advanced Materials* **2007**, *19*, 1105–1108.

[34] Zuloaga, J.; Nordlander, P. *Nano letters* **2011**, *11*, 1280–3.

[35] Messinger, B.; Von Raben, K.; Chang, R.; Barber, P. *Physical Review B* **1981**, *24*, 649.

[36] Curto, A. G.; Volpe, G.; Taminiau, T. H.; Kreuzer, M. P.; Quidant, R.; van Hulst, N. F. *Science (New York, N.Y.)* **2010**, *329*, 930–3.

[37] Anker, J. N.; Hall, W. P.; Lyandres, O.; Shah, N. C.; Zhao, J.; Van Duyne, R. P. *Nature Materials* **2008**, *7*, 442–53.

[38] Claridge, S. A.; Liang, H. W.; Basu, S. R.; Fréchet, J. M. J.; Alivisatos, A. P. *Nano Letters* **2008**, *8*, 1202–1206.

[39] Lee, J.; Hernandez, P.; Lee, J.; Govorov, A. O.; Kotov, N. A. *Nature Materials* **2007**, *6*, 291–5.

[40] Fedutik, Y.; Temnov, V.; Schöps, O.; Woggon, U.; Artemyev, M. *Physical Review Letters* **2007**, *99*, 1–4.

[41] Slot, J. W.; Geuze, H. J. *European Journal of Cell Biology* **1985**, *38*, 87–93.

[42] Brown, K. R.; Walter, D. G.; Natan, M. J. *Chemistry of Materials* **2000**, *12*, 306–313.

[43] Gersten, J.; Nitzan, A. *The Journal of Chemical Physics* **1981**, *75*, 1139–1152.

List of Publications

"Exciton–Plasmon Interactions in Quantum Dot–Gold Nanoparticle Structures" Eyal Cohen-Hoshen, Garnett W. Bryant, Iddo Pinkas, Joseph Sperling, and Israel Bar-Joseph *Nano Letters* **2012** 12 (8), 4260-4264 .

"Self-assembly of metallic double-dot single-electron device" A. Guttman, D. Mahalu, J. Sperling, E. Cohen-Hoshen, and I. Bar-Joseph *Appl. Phys. Lett.* **2011** 99, 063113 .

Declaration

I declare that the thesis summarizes my independent research. A Collaboration was performed in the form of discussion and numerical calculations with Dr. Garnett Bryant from NIST.

Appendix

The paper **"Exciton–Plasmon Interactions in Quantum Dot–Gold Nanoparticle Structures"** was published in June 2012.

NANO LETTERS

Letter

pubs.acs.org/NanoLett

Exciton–Plasmon Interactions in Quantum Dot–Gold Nanoparticle Structures

Eyal Cohen-Hoshen,*[,†] Garnett W. Bryant,[‡] Iddo Pinkas,[§] Joseph Sperling,[∥] and Israel Bar-Joseph[†]

[†]Department of Condensed Matter Physics, Weizmann Institute of Science, Rehovot 76100, Israel

[‡]Quantum Measurement Division, National Institute of Standards and Technology, 100 Bureau Drive, Stop 8423, Gaithersburg, Maryland 20899-8423, United States

[§]Department of Chemical Research Support, Weizmann Insitute of Science, Rehovot 76100, Israel

[∥]Department of Organic Chemistry, Weizmann Institute of Science, Rehovot 76100, Israel

S *Supporting Information*

ABSTRACT: We present a self-assembly method to construct CdSe/ZnS quantum dot–gold nanoparticle complexes. This method allows us to form complexes with relatively good control of the composition and structure that can be used for detailed study of the exciton–plasmon interactions. We determine the contribution of the polarization-dependent near-field enhancement, which may enhance the absorption by nearly two orders of magnitude and that of the exciton coupling to plasmon modes, which modifies the exciton decay rate.

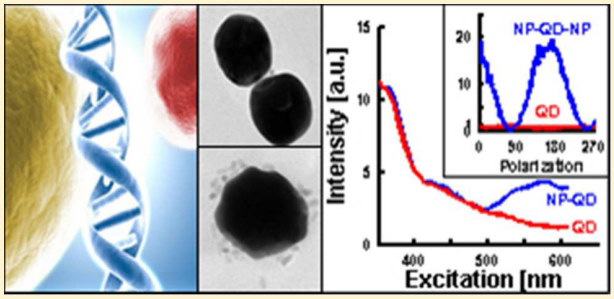

KEYWORDS: *Quantum dot, nanocrystal, gold nanoparticle, plasmon, exciton, self-assembly, CdSe/ZnS, DNA*

The controlled coupling of a quantum emitter (QE) to a metal nanoparticle (NP) is one of the most challenging yet promising goals in plasmonics. This coupling profoundly affects the QE absorption and emission rates, and, hence, by controlling the design of a QE-NP structure one can tailor the optical properties of the system. The mechanisms through which these rates are affected by the QE-NP coupling are different. The QE absorption changes due to the local field enhancement near the NP,[1,2] while its emission is modified due to the interaction between the QE dipole and the plasmons in the NP. This interaction may lead to an enhanced radiative rate when dipole modes are excited in the metal and to emission quenching when higher multipoles are excited.[1,3]

Many studies of QE-NP interactions were conducted with organic molecules as the emitter. The ease of attaching these molecules to metal surfaces, by direct bonding or through an intermediate ligand, has triggered a wealth of studies of this system.[4−7] However, organic molecules are characterized by a large overlap between the absorption and emission spectra, and it is therefore difficult to isolate the changes which are due to absorption enhancement from those related to emission changes.[4] This gives rise to a large scatter in the reported results[3−6,8−10] and limits our insight into the behavior of the system.

Semiconductor quantum dots (QDs) offer several advantages in this context.[10−14] Their absorption spectrum extends over a broad range, and it is simple to overlap it with the spectrum of NP plasmon of various sizes and material systems. The emission spectrum, on the other hand, is narrow and well-separated from the absorption. In fact, it is typically narrower than that of the plasmon, and therefore by selecting QDs of different sizes one can tune the exciton emission across the plasmon resonance. Finally, the strong oscillator strength associated with the QD exciton allows performing single object experiments easily. Indeed, the formation of a QD-NP system has been a subject of growing interest in the past decade. The straightforward approach to realize this system is based on using a scanning probe. In this approach the QD-NP distance was controlled either by moving a NP on a substrate with QDs using an atomic force microscopy (AFM) tip[15] or by using the metallic AFM tip itself as the plasmonic structures.[16] Other approaches have used patterned metallic substrates to define the plasmonic structure. The QDs are either distributed uniformly[17] or positioned in prepatterned locations.[13,18]

In this work we present a method to construct QD-NP complexes, which is based on the self-assembly of gold NPs and CdSe/ZnS QDs.[19−21] The QD-NP distance in these complexes is defined by an intermediate DNA molecule, through the number of DNA basepairs.[22] This method allows us to form complexes with relatively good control of the composition and structure that can be used for a detailed study of the QE-NP coupling. We determine the plasmonic effect on the QDs absorption and separate it from the changes in the emission. We find that when the incident polarization is changed from

Received: May 22, 2012
Revised: June 26, 2012
Published: June 27, 2012

   dx.doi.org/10.1021/nl301917d | *Nano Lett.* 2012, 12, 4260−4264

being aligned along with to being perpendicular to the QD-NP axis the QD absorption may change dramatically, by nearly 2 orders of magnitude in NP-QD-NP structures, thus offering an effective tool for controlling the emission of these objects.

The schematic structure of the QD-NP complexes that we study is illustrated in Figure 1. We start with commercially

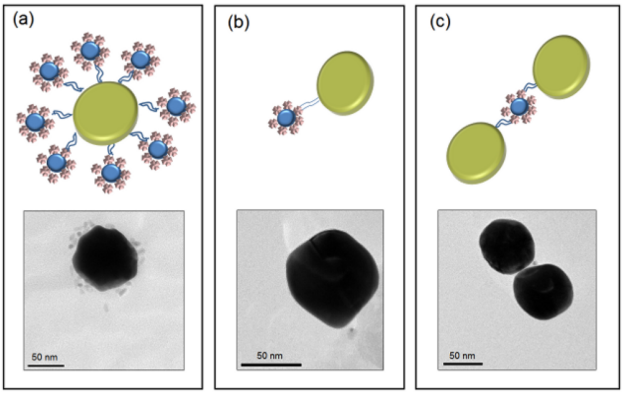

Figure 1. QD-NP complexes studied in this work. The QDs (blue spheres) are surrounded by streptavidin molecules and are connected by an intermediate biotin-dsDNA-thiol molecule to 80 nm gold NPs (yellow spheres). (a) Multiple QDs attached to a single gold NP, (b) a single QD attached to a single gold NP, and (c) a single QD having two DNA strands in between two gold NP (all scale bars are 50 nm.).

available CdSe/ZnS QDs covered with streptavidin (Invitrogen) and suspended in aqueous solution. The gold NPs are prepared in a two-stage process: 17 nm gold nanoparticles are prepared by citrate reduction of gold precursors in the presence of tannic acid.[21] These NPs are used as seeds for the growth of larger spherical NP in three steps, using hydroxyl amine as the reducing agent (see Supporting Information for this letter). The NP diameter is selected to be 80 nm throughout this work. This relatively large size gives rise to strong plasmonic effects, which are typically proportional to the NP volume and hence facilitate the measurements. To link the QDs to the gold NPs we use thiol-DNA-biotin molecules: the thiol end of the molecule covalently binds to the surface of the gold NP, while the biotin end binds to the streptavidin on the QD. By controlling the QD to NP ratio we can form structures that consist of one or multiple QDs that are attached to a single NP (Figure 1a,b). When a few DNA molecules are attached to a single QD we can obtain structures where several NPs are connected to a single QD, in particular NP-QD-NP structure (Figure 1c). We select the desired complex from the solution using gel electrophoresis separation.[19] The full description of all of the synthesis processes is available in the Supporting Information for this letter.

A key aspect of our studies is the use of photoluminescence excitation (PLE) measurements as the method to obtain the QD absorption: We scan the exciting wavelength continuously over a broad range and measure the emission spectrum (Figure 2a). The changes in the integrated emission intensity as a function of excitation wavelength is proportional to the absorption spectrum. This method allows us to isolate the absorption spectrum of the QD from other processes that occur in parallel in the solution, primarily resonant scattering. We perform these measurements using a Jobin Yvon Fluorolog-3 spectrofluorometer system.

Figure 2b shows a comparison between the PLE spectrum of a solution of NPs connected to multiple QDs (Figure 1a) and a solution of bare QDs. To be able to compare the two, we normalize the spectra such that the emission intensity of the two solutions under excitation at 350 nm coincides. It is seen that the two spectra lie precisely on each other over a broad spectral range (350−480 nm) and separate as the excitation energy approaches the plasmon resonance wavelength at 560 nm. The absorption enhancement at the plasmon resonance is clearly visible.

To determine the enhancement factor we simply divide the QD-NP spectrum by that of the bare QD, and the results are shown in Figure 2c. We perform this measurement on different QDs, with emission wavelengths ranging between 565 nm and 655 nm, and observed very similar enhancement factors, ranging between 3 and 4. To compare our results with theory we calculate the local field enhancement factor as a function of the excitation wavelength for this geometry, averaging over the different incident light polarization. We use the boundary element method[23] to perform fully retarded electromagnetic calculations of QD-NP and NP-QD-NP structures. Near-field intensities, dependence on excitation polarization, ensemble averages, and decay rates of a dipole embedded in the dot are determined. It is seen that the calculated wavelength dependence of the enhancement is in a very good agreement with our measurement. In particular, the measured 4-fold enhancement agrees nicely with a 10 nm gap (Figure 2d). This length is the expected gap in our structure, which consists of 20 base-pairs of double-stranded DNA (6 nm) and a streptavidin tetramer (4 nm), and is verified in transmission electron microscopy (TEM) imaging. We have conducted experiments with smaller NPs, with 40 and 60 nm diameters, and observed a smaller enhancement, as expected from theory. Previously published measurements of plasmon enhancement have given enhancement factors that span a large range.[3−6,8−10] Our experiment resolves this ambiguity and gives a quantitative value for the enhancement factor.

To obtain a complete picture of the QD-NP interaction, we conduct time-resolved measurements of the QD exciton emission. Figure 2e compares the emission lifetime of bare QD and QD-NP solutions, with peak emission at 605 nm. The bare QD lifetime could be easily resolved within our time resolution and is found to be 17 ns. It is seen that the QD-NP lifetime is much shorter and is comparable to our time resolution. Using an iterative fitting process, in which the measured system response is convolved with exponential decay rates, the QD-NP data could best be fit to two exponential decay rates of 0.3 and 1.4 ns. Figure 2f shows the calculated enhancement of the decay rates for a 10 nm gap QD-NP structure. It is seen that the total decay rate, which is the sum of the radiative and nonradiative rates, increases by more than an order of magnitude at 605 nm, in good agreement with the observed result. We note that both rates should be enhanced in the QD-NP structure relative to the bare QD, and the quantum efficiency, which is the fraction of the radiative rate from the total, becomes approximately 0.5 at 600 nm, and may go down to 0.05 at 520 nm.

The solution measurements described above are insensitive to the incident polarization. To study this aspect we conduct measurements of single objects, consisting of a gold NP attached to a single CdSe/ZnS QD (Figure 1b). This experiment is performed using an inverted Nikon TI-E microscope in an epifluorescence configuration. The objects

dx.doi.org/10.1021/nl301917d | Nano Lett. 2012, 12, 4260−4264

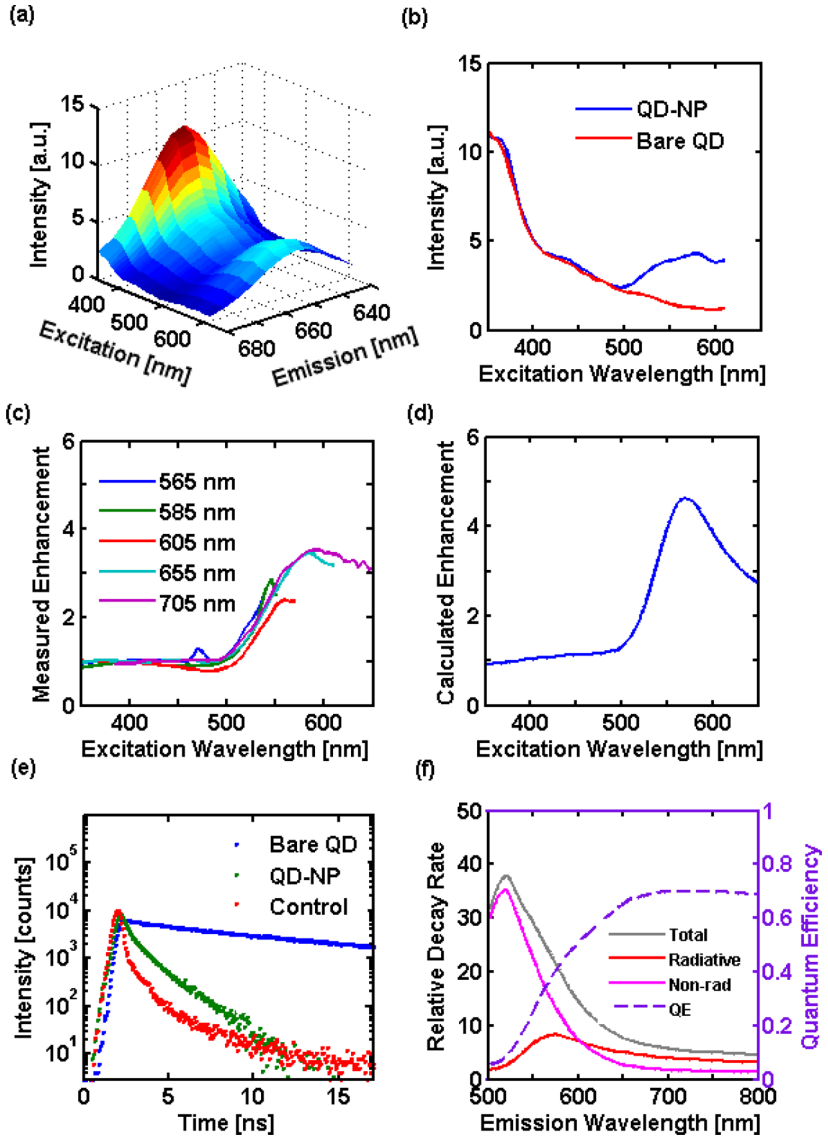

Figure 2. Photoluminescence excitation (PLE) and lifetime measurements of aqueous solutions containing complexes of multiple QDs attached to single gold NPs. (a) The emission intensity as a function of excitation and emission wavelengths. (b) A comparison between the PLE spectra of QD-NP structures and bare QDs (the PL intensity is measured at 655 nm). The plasmon enhancement of the QD absorption around 560 nm is clearly visible. (c) The enhancement spectrum of various QD-NP structures emitting at 565, 585, 605, 655, and 705 nm. (d) A calculation of the average near field enhancement spectrum for a QD-NP structure (5 nm QD, 80 nm NP, 10 nm spacing). (e) The decay time of bare QDs (blue) and QD-NP structures (green; the system response is shown in red). The large decrease of the decay time in the QD-NP structures is clearly visible. (f) The radiative and nonradiatiative decay rate of QD-NP (relative to a bare QD) and the quantum efficiency as function of the emission wavelength.

are dispersed on a microscope coverslip and are immersed in water. They are illuminated by a 532 nm laser (1 μW) focused to a tight spot (2 μm diameter), and the collected light intensity is measured by an imaging spectrometer (Andor SR-303i) and an EM-CCD (Andor Ixon^{EM}+ 897). We verified by SEM imaging that the objects are well-dispersed, and the typical distance between them is much larger than the excitation spot. Figure 3a shows a typical emission spectrum of a single QD measured in this system (red line). It is clearly seen that the spectrum of this single object is significantly narrower than that obtained in a solution measurement (gray line), reflecting the size distribution of the QDs in a solution.

We measure 50 bare QDs and compare their emission intensity to that of a similar number of QD-NP. We find that the QD-NP ensemble exhibits a significantly broader distribution of intensities. The uniformity of our reaction products, NP and QD size as well as the QD to NP separation, suggests that the large variability in emission intensity does not originate from inhomogeneity of the objects but is rather fundamental. We show below that the reason for this variability is the random orientation of the symmetry axis of the various QD-NP objects relative to the laser polarization.

Figure 3b shows the emission intensity of a single QD-NP object as the excitation polarization angle is varied. It is seen that the intensity exhibits a clear and reproducible sinusoidal dependence on the polarization angle. We took special care to verify that this dependence does not originate from a measurement artifact, such as slight movement of the excitation spot with the rotation of the polarization. Indeed, the maximum for different objects appears at different angles. This proves that

dx.doi.org/10.1021/nl301917d | *Nano Lett.* 2012, 12, 4260−4264

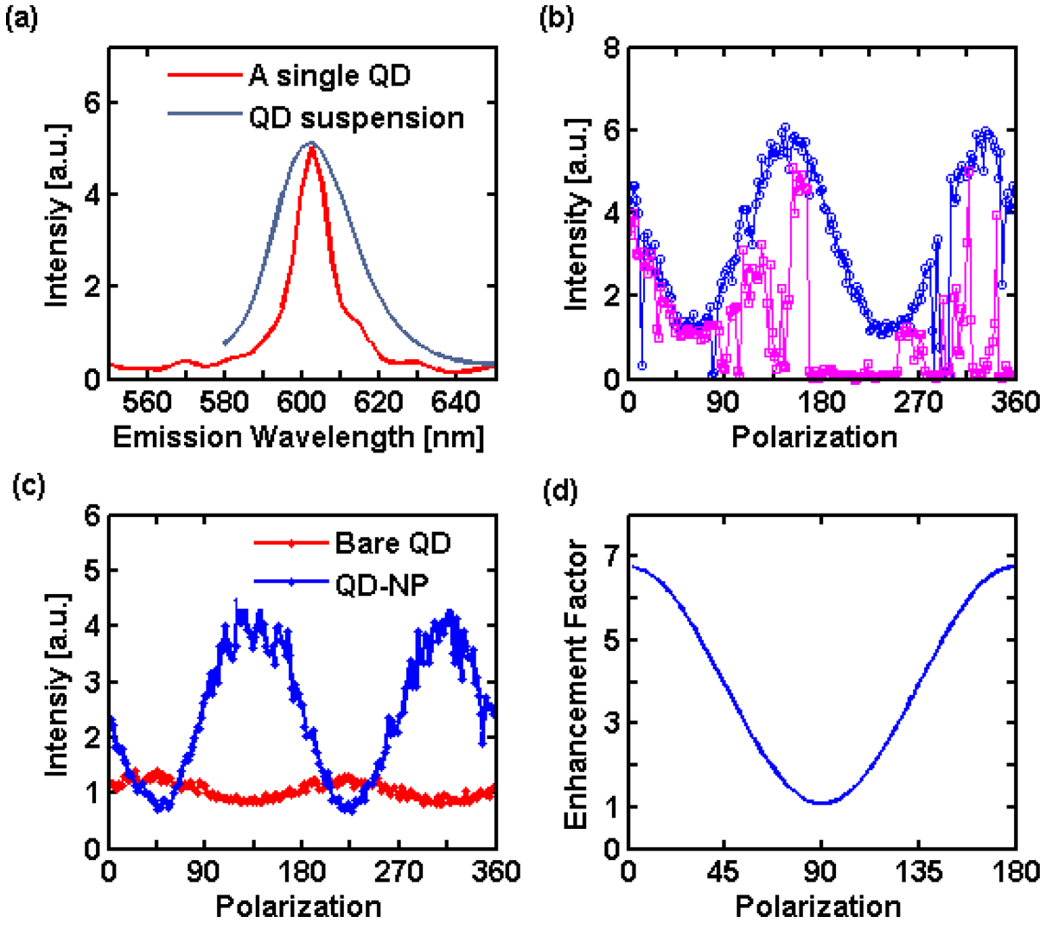

Figure 3. Single object measurements. (a) A comparison of the measured emission spectrum of a single QD and of a solution of QDs. (b) Two consecutive measurements (blue and pink) of the emission intensity of a single QD while continuously varying the excitation polarization. (c) The emission intensity as a function of laser polarization for a single QD-NP and a bare QD. The data are taken by performing five consecutive measurements as in b and taking the "high" values. (d) The calculated near field enhancement factor for a QD-NP structure (5 nm QD, 80 nm NP,10 nm spacing) as a function of the excitation polarization angle with respect to the axis connecting the QD and the NP.

the observed dependence is due to the relative orientation of the QD-NP axis relative to the laser polarization. It is seen that the sample shows emission intermittency, which is a characteristic of a single QD measurement, and in the following we consider the highly emitting state only.

Figure 3c compares the polarization dependence of a bare QD and a single QD-NP. We present the curve of a QD-NP object, which exhibits the largest contrast, presumably because its axis is parallel to the coverslip plane. Objects that are oriented at an angle to this plane would have lower polarization dependence. We note that there is a weak polarization dependence also in the bare QDs measurement. This is probably related to an asymmetry in the QD shape.[24,25] The sinusoidal dependence of the QD-NP objects agrees well with the expected plasmonic behavior: the near field around the metal sphere is maximal along the laser polarization axis, and minimal perpendicular to it. As we rotate the laser polarization we move the maxima and minima around the NP, and consequently modify the local field experienced by the QD. At the peak of the curve we find that the emission intensity of the QD-NP is enhanced relative to the bare QD, by approximately a factor of 4, while the intensity at the minimum is suppressed. Figure 3d shows the calculated polarization dependence of the enhancement factor for a 10 nm gap. It is seen that the contrast ratio between minimum and maximum values, which is approximately 7, agrees very well with that found experimentally. This calculation describes only the enhancement of the local field at the QD. The measured emission intensity is a product of this enhancement curve and the modified quantum efficiency, which is ~0.5 at this wavelength (Figure 2f).

The strong polarization sensitivity is further enhanced in the NP-QD-NP structure (Figure 1c). Figure 4a shows the polarization dependence of the emission intensity for a single NP-QD-NP object and compares it to a bare QD (its average is taken to be 1). Again, a sinusoidal dependence is observed, but this time with a contrast ratio, which is close to 100. Figure 4b shows a calculation of the near field intensity for this structure. We find that the contrast ratio is maximal when the QD is located on the axis between the spheres and drops as the QD shifts away from this axis. This maximum is close to 100 for the parameters of our sample, in a very good agreement with our findings. This observation demonstrates the strength of plasmonic structure design in tailoring the optical properties of a quantum emitter.

In conclusion, our measurements provide quantitative insight into the various mechanisms affecting the plasmon coupled QD emission. In particular, we separate the contribution of the near field enhancement near the NP, which gives rise to an increase

dx.doi.org/10.1021/nl301917d | *Nano Lett.* 2012, 12, 4260−4264

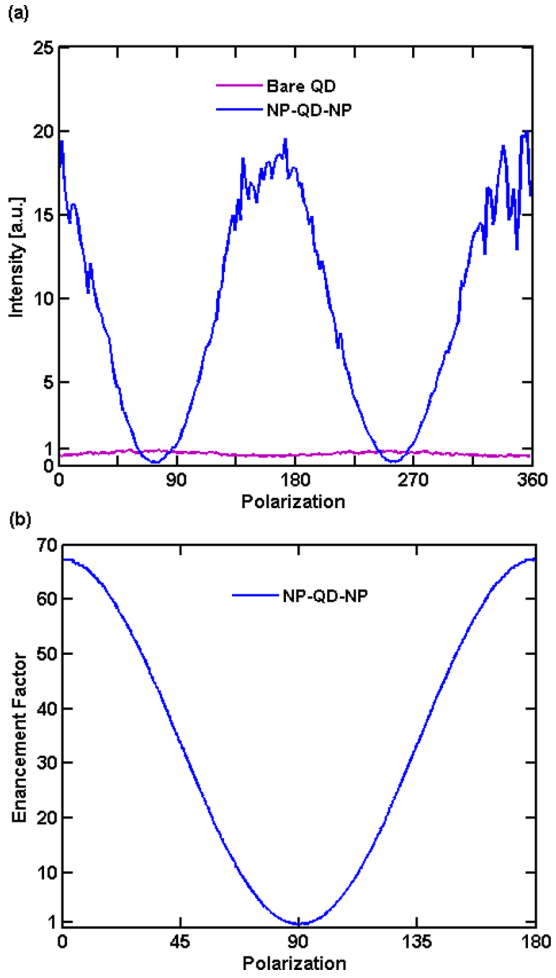

Figure 4. NP-QD-NP structure measurements. (a) Emission intensity of a single NP-QD-NP structure as a function of the polarization angle. We obtain up to 20-fold enhancement with respect to a typical bare QD, and there is 85:1 contrast between the maximal intensity to the minimal intensity. (b) Calculated near field enhancement for a NP-QD-NP structure (5 nm QD, 80 nm NP, 5 nm spacings).

of the absorbed power in the QD, and that of the exciton-plasmon interaction, which modifies the decay rates and the corresponding quantum efficiency. We show that the self-assembly of QD-NP complexes by the highly specific biotin–avidin interaction and the use of DNA molecules as a spacer provide us with a useful tool for controlling quantum emitter–plasmon interaction.

■ ASSOCIATED CONTENT

Ⓢ Supporting Information

Further details of the experimental procedures. This material is available free of charge via the Internet at http://pubs.acs.org.

■ AUTHOR INFORMATION

Corresponding Author

*E-mail: Eyal.Cohen-Hoshen@weizmann.ac.il.

Notes

The authors declare no competing financial interest.

■ ACKNOWLEDGMENTS

This research was supported by the Israel Science Foundation. All mention of product names is done to provide a complete description of this work. This does not imply a validation or endorsement of these products by NIST.

■ REFERENCES

(1) Metiu, H. *Prog. Surf. Sci.* **1984**, *17*, 153–320.
(2) Maier, S. A. *Plasmonics: Fundamentals and Applications*; Springer: New York, 2007.
(3) Mertens, H.; Koenderink, A.; Polman, A. *Phys. Rev. B* **2007**, *76*, 1–12.
(4) Anger, P.; Bharadwaj, P.; Novotny, L. *Phys. Rev. Lett.* **2006**, *96*, 3–6.
(5) Lakowicz, J. R. *Plasmonics (Norwell, Mass.)* **2006**, *1*, 5–33.
(6) Zhang, J.; Fu, Y.; Chowdhury, M. H.; Lakowicz, J. R. *Nano Lett.* **2007**, *7*, 2101–7.
(7) Anker, J. N.; Hall, W. P.; Lyandres, O.; Shah, N. C.; Zhao, J.; Van Duyne, R. P. *Nat. Mater.* **2008**, *7*, 442–53.
(8) Govorov, A. O.; Bryant, G. W.; Zhang, W.; Skeini, T.; Lee, J.; Kotov, N. A.; Slocik, J. M.; Naik, R. R. *Nano Lett.* **2006**, *6*, 984–994.
(9) Lee, J.; Govorov, A. O.; Dulka, J.; Kotov, N. A. *Nano Lett.* **2004**, *4*, 2323–2330.
(10) Shimizu, K.; Woo, W.; Fisher, B.; Eisler, H.; Bawendi, M. *Phys. Rev. Lett.* **2002**, *89*, 9–12.
(11) Fedutik, Y.; Temnov, V.; Schöps, O.; Woggon, U.; Artemyev, M. *Phys. Rev. Lett.* **2007**, *99*, 1–4.
(12) Mertens, H.; Biteen, J. S.; Atwater, H. A.; Polman, A. *Nano Lett.* **2006**, *6*, 2622–5.
(13) Curto, A. G.; Volpe, G.; Taminiau, T. H.; Kreuzer, M. P.; Quidant, R.; van Hulst, N. F. *Science (New York, N.Y.)* **2010**, *329*, 930–3.
(14) Lee, J.; Hernandez, P.; Lee, J.; Govorov, A. O.; Kotov, N. A. *Nat. Mater.* **2007**, *6*, 291–5.
(15) Ratchford, D.; Shafiei, F.; Kim, S.; Gray, S. K.; Li, X. *Nano Lett.* **2011**, *11*, 1049–54.
(16) Farahani, J. N.; Pohl, D. W.; Eisler, H.-J.; Hecht, B. *Phys. Rev. Lett.* **2005**, *95*, 017402.
(17) Pompa, P. P.; Martiradonna, L.; Torre, A. D.; Sala, F. D.; Manna, L.; De Vittorio, M.; Calabi, F.; Cingolani, R.; Rinaldi, R. *Nat. Nanotechnol.* **2006**, *1*, 126–30.
(18) Jun, Y. C.; Pala, R.; Brongersma, M. L. *J. Phys. Chem. C* **2010**, *114*, 7269–7273.
(19) Claridge, S. A.; Liang, H. W.; Basu, S. R.; Fréchet, J. M. J.; Alivisatos, A. P. *Nano Lett.* **2008**, *8*, 1202–1206.
(20) Brown, K. R.; Walter, D. G.; Natan, M. J. *Chem. Mater.* **2000**, *12*, 306–313.
(21) Slot, J. W.; Geuze, H. J. *Eur. J. Cell Biol.* **1985**, *38*, 87–93.
(22) Gueroui, Z.; Libchaber, A. *Phys. Rev. Lett.* **2004**, *93*, 166108.
(23) Aizpurua, J.; Bryant, G. W.; Richter, L. J.; Garca de Abajo, F. J. *Phys. Rev. B* **2005**, *71*, 235420-1–234520-13.
(24) Suo, B.; Su, X.; Wu, J.; Chen, D.; Wang, A.; Guo, Z. *Mater. Chem. Phys.* **2010**, *119*, 237–242.
(25) Acharya, S.; Panda, A.; Efrima, S.; Golan, Y. *Adv. Mater.* **2007**, *19*, 1105–1108.

Exciton-Plasmon Interactions in Quantum Dot – Gold Nanoparticle Structures – Supporting Information

Eyal Cohen-Hoshen,[*,†] Garnett W. Bryant,[‡] Iddo Pinkas,[¶] Joseph Sperling,[§] and Israel Bar-Joseph[†]

Department of Condensed Matter Physics, Weizmann Institute of Science, Israel, Quantum Measurement Division, National Institute of Standards and Technology, 100 Bureau Drive, Stop 8423, Gaithersburg, Maryland 20899-8423, Department of Chemical Research Support, Weizmann Insitute of Science, Israel, and Department of Organic Chemistry, Weizmann Institute of Science, Israel

E-mail: Eyal.Cohen-Hoshen@weizmann.ac.il

All reagents were used as received from Sigma-Aldrich. All DNA oligo-nucleotides were obtained from Integrated DNA Technologies (IDT). We used CdSe/ZnS streptavidin quantum dots from Invitrogen (Qdots Invitrogen). Gel electrophoresis sample extraction kit was obtained from Gebaflex technologies. DI water (18.3 MΩcm^{-1}) was used in all experiments.

[*]To whom correspondence should be addressed

[†]Department of Condensed Matter Physics, Weizmann Institute of Science, Israel

[‡]Quantum Measurement Division, National Institute of Standards and Technology, 100 Bureau Drive, Stop 8423, Gaithersburg, Maryland 20899-8423

[¶]Department of Chemical Research Support, Weizmann Insitute of Science, Israel

[§]Department of Organic Chemistry, Weizmann Institute of Science, Israel

1 Gold NP synthesis

1.1 17 nm gold NP Synthesis

A 20 ml solution of 0.2% w/v Na3-Citrate + 25 µl of 1% w/v Tannic Acid heated to 600 C is added under vigorous stirring to a solution which consists of 1 ml of 1% w/v NaAuCl4 diluted to 80 ml DI water. The solution is heated to boil and is then boiled for another 10 minutes and cooled to room temperature.

1.2 80nm gold NP synthesis

1 ml of 17 nm gold NP solution is put in a 50 ml plastic falcon tube.

1. 1 ml of 0.01% NaAuCl4 is added under stirring on vortex.
2. Sequentially 40 µl of 40 mM hydroxyl amine is added under vigorous stirring.
3. Steps 1-2 are repeated until a volume of 10 ml is reached.
4. The NP solution is transferred to an erlenmeyer, heated to boil, boiled for 10 min and cooled to room temperature.
5. Steps 1-2 are repeated until a volume of 100 ml is reached, on a magnetic stirrer.
6. BSPP (bis-P-sulfonatophenylphosphine) is added to the solution with a final concentration of 93 mM and left overnight at room temperature.

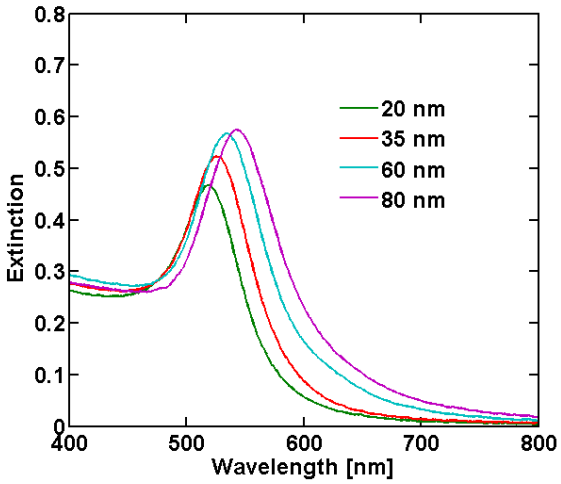

Figure 1: The Extinction spectra of NP different sizes for the above reaction.

2 QD-NP conjugates Synthesis

2.1 DNA Hybridization:

DNA sequences:

- **Sequence 1**- 5'-biotin-GCAGTAACGC TATGTGACCG-3'-thiol
- **Sequence 2**- 5'-CGGTCACATA GCGTTACTGC-3'

dsDNA - Sequence 1, and **Sequence 2** at a concentration of 0.5 mM are mixed in a 1:1 ratio, reacted with with TCEP (tris-carboxyethylphosphine) with a final concentration of 5 mM TCEP and stirred on vortex. The solution is left for at least 20 min for hybridization at room temperature and then diluted to 1 µM in DI water.

2.2 QD-DNA hybrids:

Streptavidin coated QD (Qdots Invitrogen) emitting at 565 nm,585 nm ,605 nm, 655 nm and 705 nm, at a concentration of 1 µM are reacted with **dsDNA** at 1:1 ratio (for NP-QD conjugates) ratio and at 1:2 ratio (for NP-QD-NP conjugates).

2.3 QD-NP conjugates:

1. For creating structures having multiple QDs and a single gold NP, QD-DNA hybrids (1:1 QD:DNA) are added to 80 nm gold NP solution at 100:1 ratio at equal volumes. After overnight at room temperature the excess unreacted QD-DNAs are separated with 6 cycles of centrifugation and resuspension after removing the supernatant (600g at a benchtop centrifuge for 5 minutes.)

2. For creating structures having a single QD attached to a single gold NP, QD-DNA hybrids (1:1 QD:DNA) are reacted with NPs at 1:1 ratio.

3. For creating structures having a single QD attached between two gold NP, QD-DNA hybrids (1:2 QD:DNA) are reacted with NPs at 1:2 ratio.

4. The reaction products of 2. and 3. are purified by gel electrophoresis using 1% agarose with a 1/2xTBE in a current of 40 mamps. The desired are cut from the gel and are extracted using dialysis micro tubes (Geba-Flex microtubes dialysis kit). A small fraction of the products is examined by TEM.

The selection of the reaction products was done in the following manner:

Complexes consisting of NPs with many QDs were prepared in a process where the solution is saturated with QDs. The challenge here is to separate them from the non-reacting QDs, and this is done by six cycles of centrifuging, and not by electrophoresis (2.3.1). Gel electrophoresis was used to separate between NP-QD and NP-QD-NP objects. This is relatively straightforward as evidenced by the image below, which clearly shows the two bands. The lower band contains also a small fraction of single NP with more than one QDs. These objects can't be separated using this method; however, they are rare and easily identified in the optical measurements: their polarization dependence shows a-periodicity.

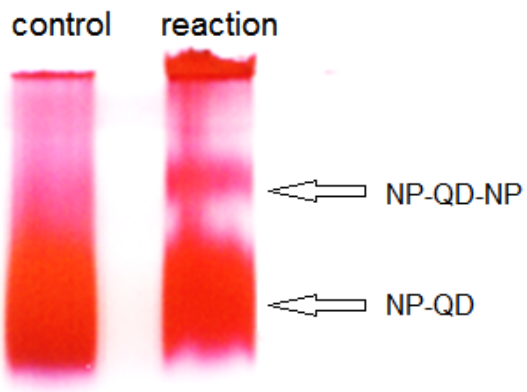

3 Characterization and Measurement.

3.1 TEM

TEM images were acquired using a Philips CM-120 TEM in bright mode. Grids 400 mesh were purchased from TED Pella inc.

Obtaining an ensemble image of the complexes is not simple. The first difficulty comes from the fact that a 5 nm diameter CdSe/ZnS QD attached to a single 80 nm NP could be seen in TEM only if the NP-QD axis is parallel to the grid. At a different orientation the high absorbing gold NP hides the CdSe/ZnS. Thus, a zoom out view typically shows the NP, and only a careful search reveals the QD. The second problem is more technical: to obtain many particles in the field of view one needs to have a high concentration of objects in the applied solution. However, this typically gives rise to particle aggregation upon drying on the surface of the TEM grid. The image below shows such an aggregate that is formed under high concentration, and after drying. Hence, for the TEM imaging we worked with low concentration solutions.

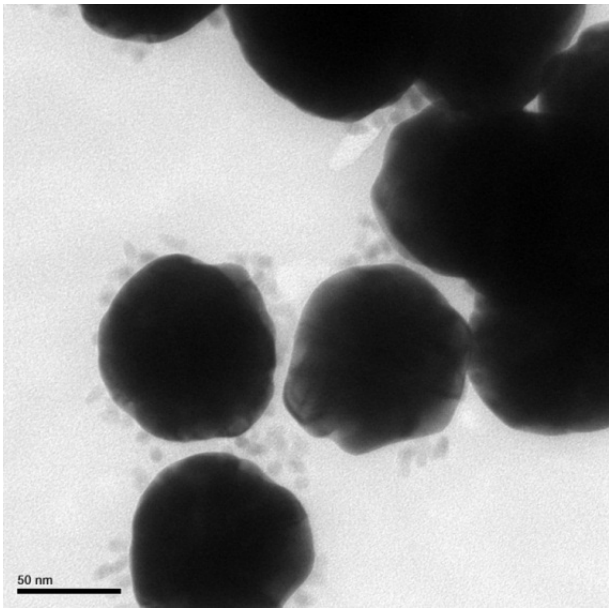

In order to determine the yield of the process we ran a similar reaction with 20 nm diameter NPs. In this case the ratio between the NP diameter, the DNA length and the QD diameter is more favorable, and it is much easier to resolve the QD in the TEM images. Our measurements show a relatively high yield: 90% (out of 40 objects) for NP-QD (second band), and around 50% for NP-QD-NP (third band).

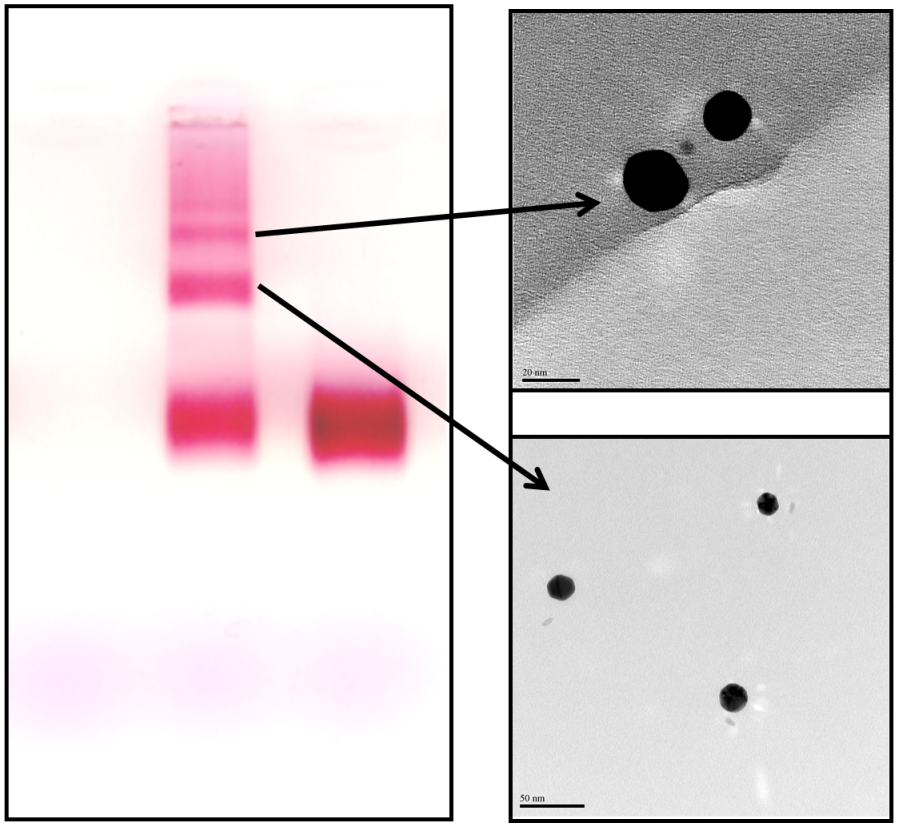

3.2 Single Objects Optical Measurements

Optical measurements on single objects were performed on an inverted Nikon microscope in an epifluorescence configuration. We use an oil immersion X60 1.4NA objective and a 532 nm laser excitation (Cobbolt Samba-532 diode laser). The polarization of the laser is varied with a Newport PR-950 polarization rotator. Collected light is dispersed by an imaging spectrometer (Andor SR-303i) and collected by an EMCCD (Andor ixonEM+897). The beam profile is characterized by illuminating a calibration sample of green ink and measuring the spatial profile of its emission. We obtain a nice Gaussian shaped focused spot, with a width of 2 μm. This width is wide enough to ensure that the illumination intensity experienced by the objects is fixed when brought to the spot center, and narrower than the average distance between the objects, such that there is a single object only in the spot. We have verified that the intensity profile does not change under the rotation of the polarization.